processes

MDPI

Article

Research on Structural Optimization and Process Parameter Response Surface Optimization of Vacuum Low-Temperature Fish Meal Dryer

Xuchu Chen [1], Wei Wang [1,*], Wuwei Feng [1], Danyu Li [2] and Rongsheng Lin [3,*]

[1] Marine Engineer Equipment College, Zhejiang Ocean University, Zhoushan 316022, China; chenxuchu1994@163.com (X.C.); fengwuwei@163.com (W.F.)
[2] Zhejiang Longyuan Sifang Machinery Manufacture Co., Ltd., Zhoushan 316014, China; info@zjlysf.com
[3] Jurong Energy (Xinjiang) Co., Ltd., Urumqi 841603, China
* Correspondence: 20230028@zjou.edu.cn (W.W.); linrongsheng@xjjurong.com (R.L.)

Abstract

To address the industry pain points of domestic traditional fish meal processing equipment, such as low protein retention, low drying efficiency, and poor operational reliability, this study focuses on high-moisture, heat-sensitive cod meal as the test material to investigate the structural improvement and synergistic optimization of process parameters for vacuum low-temperature fish meal dryers. The conventional uniform-pitch heating coil was optimized into a three-section differentiated structure, with a wear-resistant protective structure additionally incorporated to fundamentally resolve issues including insufficient heat transfer at the feed end, coking at the discharge end, and coil wear-induced leakage. Verification via COMSOL Multiphysics simulation revealed that the axial temperature gradient of the optimized equipment decreased from 8.6 °C/m to 6.2 °C/m, while the thermal fatigue life of the coil was extended from 2–3 years to over 10 years. A three-factor, three-level response surface methodology (RSM) was employed to design the experiments, with the heating temperature, vacuum degree, and drying time as independent variables and the fish meal protein content as the response variable. A total of 17 experimental runs were constructed, including 12 factorial points and 5 central points; each run was replicated three times in parallel, and data were reported as mean values. Analysis of variance (ANOVA) demonstrated that the regression model was highly statistically significant ($p < 0.0001$), with a coefficient of variation (CV) of 0.2464% and a coefficient of determination (R^2) of 0.9944, indicating excellent fitting accuracy. The determined optimal process parameters were as follows: a drying temperature of 65 °C, vacuum degree of 0.08 MPa, and drying time of 75 min. Compared with the traditional process, the optimized process shortened the drying cycle by 37.5%, reduced unit energy consumption by 29.2%, and increased the fish meal protein content by 6.6%. This research provides a reliable technical solution for the localized processing of high-end fish meal.

Keywords: vacuum drying; heat transfer; S-N fatigue; COMSOL; response surface

Check for updates

Academic Editor: César Ozuna

Received: 10 April 2026
Revised: 15 May 2026
Accepted: 15 May 2026
Published: 20 May 2026

Copyright: © 2026 by the authors. Licensee MDPI, Basel, Switzerland. This article is an open access article distributed under the terms and conditions of the Creative Commons Attribution (CC BY) license.

1. Introduction

In recent years, the rapid expansion of the global livestock industry has driven sustained growth in demand for high-quality animal protein feed. Fish meal—valued for its high protein content (typically 60–72%), low lipid content, and well-balanced profile

of essential amino acids and bioavailable trace elements—remains a cornerstone ingredient in compound feeds for terrestrial livestock and aquaculture species [1]. As both the world's largest fishing nation and one of the top livestock producers, China ranks among the leading countries in fish meal production and consumption. According to the *China Fisheries Statistical Yearbook 2024* [2], domestic fish meal output reached 659,000 metric tons in 2023, while national consumption totaled 2.237 million metric tons, approximately 73% of which was imported, primarily from Peru and Chile. However, escalating climate volatility—including marine heatwaves and anomalous sea surface temperatures—has severely disrupted anchoveta (*Engraulis ringens*) spawning cycles and recruitment, directly constraining the supply of this key raw material [3,4]. Compounding this challenge is that decades of overfishing has depleted global small pelagic stocks, prompting increasingly stringent fisheries management policies—including harvest quotas and seasonal closures—in major exporting nations [5,6]. Consequently, global fish meal production has exhibited marked volatility and an overall downward trend, exacerbating supply–demand imbalances and contributing to pronounced price instability. In this context, low-temperature vacuum drying has emerged as a promising alternative processing technology. Widely adopted in food, pharmaceutical, and fine chemical industries for thermolabile materials, it operates by reducing the system pressure below atmospheric levels to lower the boiling point (or sublimation point) of water, thereby enabling efficient moisture removal at substantially reduced temperatures [7,8]. This approach effectively mitigates thermal degradation—particularly protein denaturation and oxidation of heat-sensitive nutrients—while simultaneously enhancing drying kinetics and energy efficiency. Critically, beyond equipment design and operational configuration, process parameters—including the drying temperature, vacuum degree, and residence time—exert a decisive influence on the final product quality, especially protein retention [9]. Optimizing these parameters is therefore essential to maximize nutritional integrity without compromising throughput or economic viability.

In recent years, COMSOL has become an established tool for equipment-level optimization and mechanistic analysis in drying process engineering. Its integration with the response surface methodology (RSM) enables synergistic structural refinement and data-driven parameter tuning-informed design—thereby bridging simulation—and experimentally validated performance. Liu et al. [10] employed the heat transfer in porous media and moisture transport interfaces to model coupled heat–mass transfer during tempering of maize kernels; their simulations demonstrated that a controlled slow-cooling strategy enhanced intragranular moisture diffusion by up to 38% compared with conventional cooling. Meng et al. [11] systematically investigated the influence of the slice thickness (4–10 mm) and drying temperature (50–80 °C) on sweet potato dehydration kinetics using transient thermal–moisture simulations. The results revealed that the drying time increased from 4 h (4-mm slices) to 9.5 h (10-mm slices), while elevating the temperature from 50 °C to 80 °C at a fixed moisture ratio improved the average drying rate from 1.14 g/h to 3.20 g/h, a 181% increase. Guo et al. [12] adopted a hybrid experimental-numerical approach to characterize airflow and thermal distribution within a cabinet dryer, identifying flow dead zones and thermal stratification as key non-uniformity drivers. Their optimized configuration—featuring repositioned inlets, perforated flow-guiding baffles, and compartmentalized air chambers—reduced the velocity field non-uniformity coefficient from 24.7% to 8.3%, markedly improving drying uniformity. Wei et al. [13] examined the thermal degradation pathways in tilapia byproduct-derived fish meal, reporting optimal rehydration capacity (water absorption ratio > 4.5) within the 50–80 °C range, indicative of preserved protein matrix integrity. Most relevant to this work, Wei et al. [14] applied yjr RSM to optimize vacuum drying of fish meal, selecting the drying time, specific energy consump-

tion, and protein retention as composite response criteria. The resulting optimum—67 °C, 0.086 MPa, and 2.2 m/s hot water circulation velocity—achieved a drying time of 1085 min and a rehydration ratio of 51.03, establishing a benchmark for scalable low-temperature vacuum drying of marine protein feedstocks.

This study presents a systematic investigation into the structural optimization of a vacuum fish meal dryer, integrating COMSOL6.4—based thermomechanical coupling analysis—including transient thermal simulation and structural stress evaluation—to quantitatively characterize heat–mass transfer behavior, thermal deformation, and fatigue-prone zones under operational temperature gradients. Concurrently, experimental drying trials were conducted using high-moisture, heat-sensitive cod meal to determine its moisture desorption kinetics, critical temperature threshold for protein denaturation, and optimal process window. The synergistic integration of simulation-guided design and experimentally validated parameterization yields a robust, mechanism-informed foundation for the engineering upgrade of industrial-scale vacuum dryers.

2. Structural Optimization of the Vacuum Dryer

2.1. Core Defects at the Structural Design Level

2.1.1. Structure of the Transmission Heating Coil

Traditional equipment generally adopts the equal pitch spiral heating coil [15], as shown in Figure 1. Its structure consists of a main shaft, heating coil, shaft head, shaft head connection plate, steam inlet pipe, condensate water outlet pipe, and preheating pipe assembly. The main shaft is made of seamless steel pipe, with heating coils evenly distributed at equal intervals. To ensure uniform heating and obtain high-quality fish meal, the adjacent heating coils are spaced 180° apart. The main shaft is welded to the shaft head connection plate, and the shaft head is connected to the shaft head connection plate with bolts. Inside the main shaft, there are steam distribution pipes and condensate water check valves welded, with the inner pipes supported by inner pipe support plates. The steam distribution pipes are connected to the heating coils, allowing steam to enter the heating coils from the steam inlet pipe to heat and dry the fish meal (steam flow and structure are shown in Figure 2). During the drying of fish meal, there is heat exchange, and the steam inside the heating coils turns into condensate water. The condensate water enters the main shaft through the condensate water check valve and is discharged through the siphon pipe and the condensate water outlet pipe. Table 1 shows the list of components.

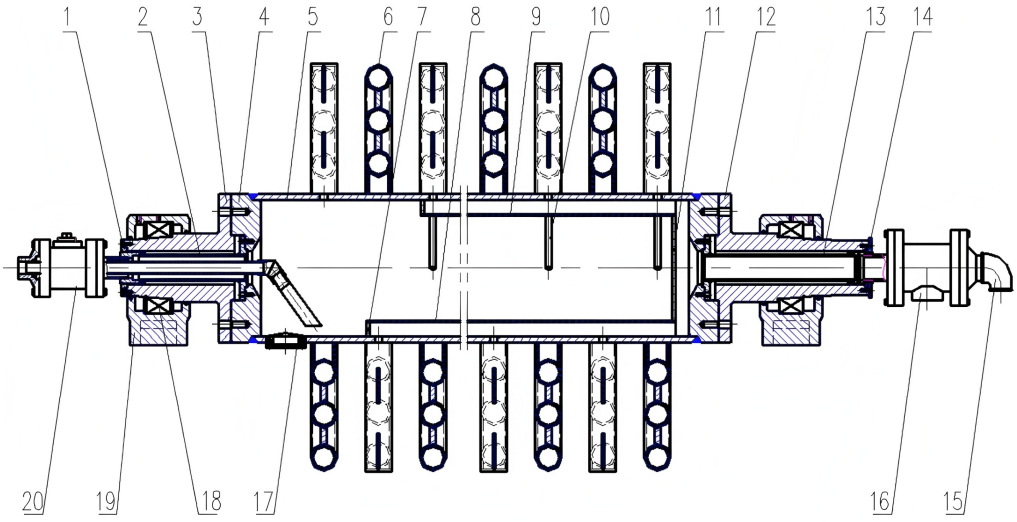
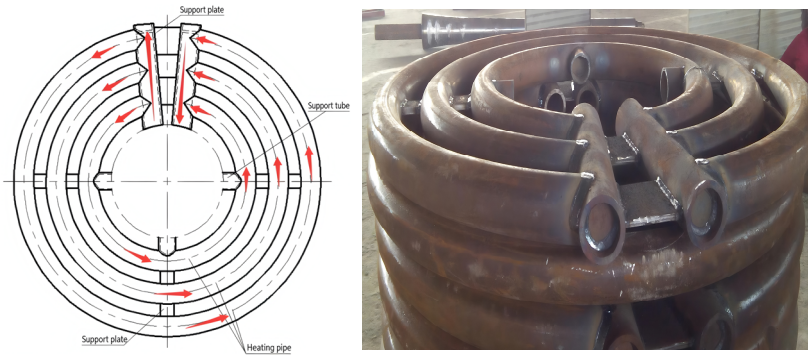


Figure 1. Traditional fish meal vacuum rake dryer.



(**a**) (**b**)

Figure 2. (**a**) Heating coil steam flow diagram. (**b**) Heating coil photograph.

Table 1. List of components and parts.

Number	Part Name	Number	Part Name	Number	Part Name
1	Non-power end shaft head flange	8	Steam inlet channel I	15	90° reducing elbow
2	Condensate water outlet pipe for the non-power end shaft head	9	Steam inlet channel II	16	Power end rotary joint
3	Non-power end journal	10	Backwater distribution pipe	17	Handhole seat
4	Shaft head connection plate	11	Main shaft head plate	18	Self-aligning roller bearing
5	Main shaft	12	Power end journal	19	Main shaft bearing housing
6	Heating coil assembly	13	Steam inlet pipe of the shaft head	20	Non-powered end rotary joint
7	Steam inlet channel cover plate	14	Power end shaft head flange		

2.1.2. Problems with the Traditional Structure

Data from actual enterprise operations show that due to the initial moisture content of wet fish meal being as high as 60–70%, a large amount of heat is required for water evaporation, resulting in a slow drying rate at the feed end—which accounts for 40–50% of the total drying time—and consequently low overall production efficiency. Overheating at the discharge end is another issue; the moisture content of fish meal in this section drops to 10–15%, making it highly temperature-sensitive (the thermal denaturation temperature range of protein is 60–80 °C). However, the uniform heat transfer structure of traditional coil heating causes the discharge-end temperature to approach 70 °C, close to the high-risk threshold for protein denaturation. Although the material temperature cannot exceed the heating steam temperature under vacuum conditions, prolonged operation may lead to local heat accumulation, causing quality defects such as surface coking and loss of bioactive proteins due to thermal denaturation.

The heating coil is in direct contact with the fish meal. Prolonged stirring and friction cause severe coil wear. In traditional equipment, the coil's average service life is only 2–3 years. Wear reduces heat transfer efficiency and poses a potential safety hazard due to leakage.

Introducing high-temperature steam directly into the vacuum drying equipment while it is still cold or allowing a rapid temperature drop after shutdown induces significant axial displacement in components such as the main shaft inner tube and the steam distribution pipe due to thermal expansion and contraction. Frequent start-stop cycles of the dryer may cause fracture and detachment of the main shaft inner tube, thereby compromising normal equipment operation.

2.2. Optimal Design of Heating Coils

2.2.1. Optimization of the Main Shaft Structure

The main shaft serves not only as a rotating shaft but also as a steam passage. Figure 3 shows two main shaft configurations: the conventional design (a) and the improved

design (b). The key distinction between them lies in the steam inlet arrangement. In design (a), steam enters from the drive end, is distributed into the main shaft's inner tubes, and then further routed through steam distribution pipes—connected to and branching from the inner tubes—before entering the heating coils to dry the fish meal. At the distal ends of the inner tubes, shaft-end seals (inner tube shaft heads) provide sealing, while support plates constrain radial movement of the inner tubes. Moreover, during a restart after shutdown, steam first flows through a dedicated preheating line to warm the internal components of the main shaft before full-flow operational steam is introduced for drying. Nevertheless, production testing reveals that exposure of the cold main shaft and its inner tubes to high-temperature steam—or rapid cooling upon shutdown—induces significant axial displacement due to thermal expansion and contraction. Frequent start-stop cycling thus risks inner tube fracture and detachment from the main shaft, leading to equipment failure. In contrast, design (b) simplifies the structure by replacing the inner tubes with an integrally welded channel–steel steam conduit. Steam enters this conduit at the drive end and flows directly to the heating coils, eliminating the risk of conduit detachment.

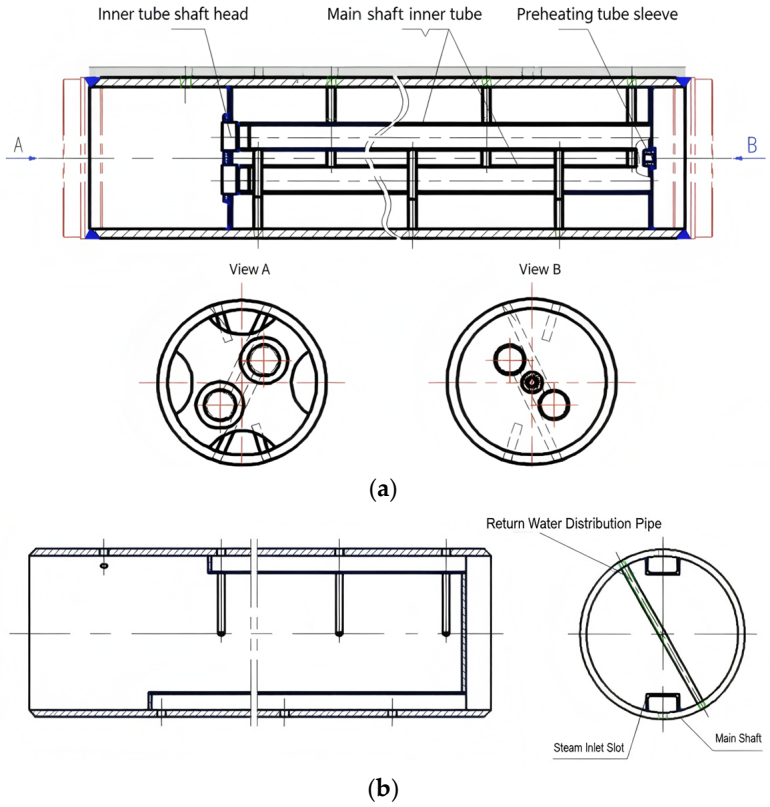


Figure 3. (**a**) Schematic diagram of the main shaft before optimization. (**b**) Optimized main shaft schematic diagram.

2.2.2. Optimization of the Heating Coil Structure

To meet the requirements of intensified heating at the feed end and reduced heating at the discharge end, the design was optimized based on the variable-pitch helical structure scheme [16,17]. The heating coil is divided axially into three sections along the vacuum chamber, with parameters tailored to each section's functional requirements, as shown in Figure 4. In the feed section (0–1 m), pitch is reduced to 80 mm; the pipe diameter is increased to 55 mm (inner diameter: 49 mm); and two additional coil turns are added, increasing the local heat transfer area and steam flow, enhancing initial heating efficiency, and accommodating the heating demand of raw material with a low initial temperature (25 °C). In the middle section (1–4 m), the standard parameters are retained (pitch: 100 mm;

pipe diameter: 50 mm; 29 turns) to ensure stable heat transfer in the core drying zone for fish meal. In the discharge section (4–5.5 m), the pitch is increased to 120 mm while the pipe diameter remains unchanged at 50 mm, thereby reducing the heat transfer area and preventing coking caused by local overheating as the fish meal approaches the final product specifications (moisture content: 10%).

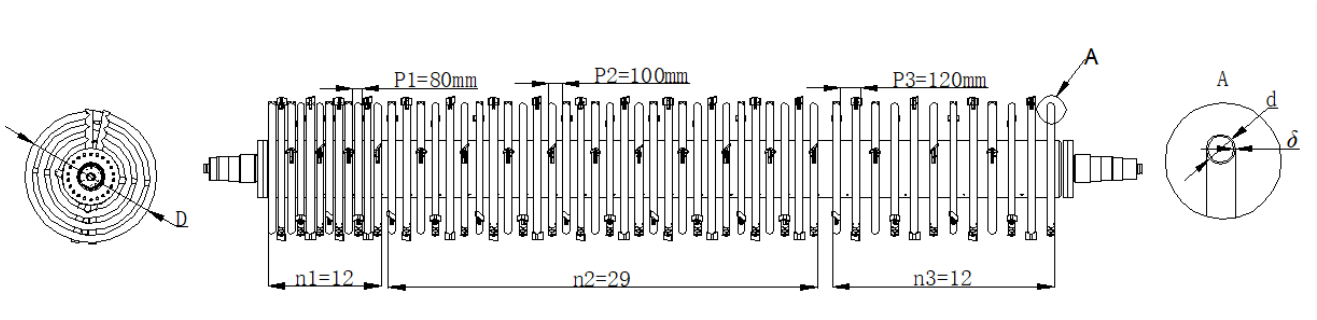


Figure 4. Simplified diagram of the optimized structure of the heating coil tube.

2.2.3. Wear-Resistant Structural Design

As shown in Figure 5, a wear-resistant ring is mounted on the outer periphery of the heating plate. When the heating plate rotates—driven by the dryer drum—the friction between the plate and the material occurs predominantly at the wear-resistant ring, thereby extending its service life. Meanwhile, the ring fully covers the outer edge's weld seam of the heating plate, preventing direct contact between the weld seam and the material. This improves the sealing integrity of the heating plate's internal cavity and enhances overall material processing performance. When the feed material contains relatively hard particles, the wear-resistant ring effectively shields the weld seam, significantly reducing the risk of mechanical damage or abrasive wear [18].

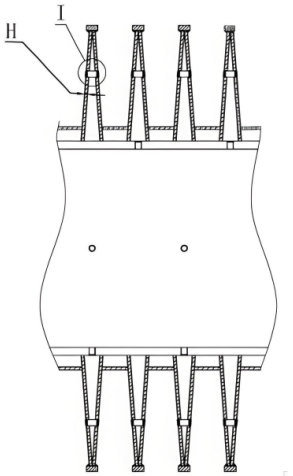


Figure 5. Structure diagram of wear-resistant ring for heated coil pipe.

The specific structure is illustrated in Figure 6. A wear-resistant ring is mounted concentrically on the outer periphery of each heating plate. The ring's width exceeds the thickness of the heating plate's outer rim. Its front face extends axially beyond the front-end face of the corresponding heating plate, and its rear face extends axially beyond the rear-end face. The ring's rear side surface is fully welded to the rear-end face of the heating plate, and its front side surface is fully welded to the front-end face. The axial cross-section of the wear-resistant ring is rectangular, and the ring is fabricated as a solid, monolithic component from stainless steel.

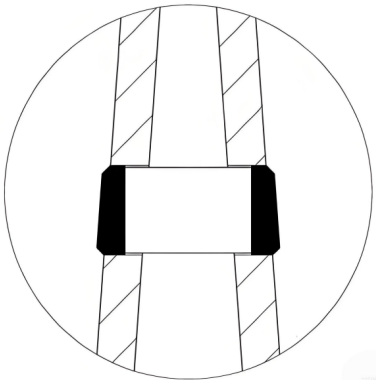


Figure 6. Wear-resistant ring.

2.3. Dimension and Parameter Verification of the Heating Coil

To quantitatively verify the heat transfer performance advantages of the three-segment differential-pitch heating coil, this section calculates the heat transfer power using the standard formula for the developed surface area of a helical cylindrical surface; compares the heat transfer characteristics of the optimized segmented coil with those of the conventional constant-pitch coil; clarifies the axial distribution pattern of heat transfer power across the three sections; and provides quantitative support for structural optimization.

2.3.1. Pipe Wall Thickness Calculation

Considering the internal pressure (p = 0.8 MPa) and abrasive wear induced by fish meal, the pipe wall thickness is determined using the thin-walled cylindrical shell strength formula [19]:

$$\delta \geq \frac{p \times d}{2 \times [\delta] \times \varnothing} \tag{1}$$

where d denotes the coil diameter, $[\delta]$ denotes the coil wall thickness, $[\sigma]$ = 130 MPa is the allowable stress of 304 stainless steel, and φ = 0.85 is the weld joint efficiency.

Then, for the coiled tubing, the minimum required wall thickness is 2.3 mm for a nominal pipe diameter of 50 mm and 2.5 mm for 55 mm. A uniform design wall thickness of 3.0 mm was adopted for both configurations to ensure structural integrity while maintaining cost-effectiveness.

2.3.2. Computational Models and Fundamental Parameters

The calculation was performed using the engineering-standard formula for the developed surface area of a helical cylinder, combined with the steady-state heat transfer equation. The governing equations are as follows:

(1) Single-turn helix expanded length:

$$L_0 = \sqrt{\left(P^2 + (\pi D)^2\right)} \tag{2}$$

(2) Coil heat transfer area (cylindrical lateral surface area):

$$A = \pi \cdot d \cdot n \cdot L_0 \tag{3}$$

(3) Steady-state heat transfer rate:

$$Q = K \cdot A \cdot \Delta T \tag{4}$$

(4) Heat transfer temperature difference:

$$\Delta T = T_1 - T_2 \tag{5}$$

In these formulae, D denotes the helix centerline diameter (0.5 m), P is the coil pitch (m), d is the coil outer diameter (m), n is the number of coil turns, K is the overall heat transfer coefficient (800 W/(m^2·°C)), T_1 is the heating steam temperature (70 °C), and T_2 is the fish meal temperature (°C). The geometric parameters of the coil configuration are illustrated in Figure 4.

The optimized coil adopts a segmented configuration comprising a 1-m feed section, a 3-m middle section, and a 1.5-m discharge section. The conventional constant-pitch coil has a fixed total of 49 turns. The material temperature is determined according to the drying characteristics of fish meal and the process requirements. The specific parameters are listed in Table 2.

Table 2. Basic calculation parameters for the heating coil.

Structural Type	Paragraphing	Axial Length, m	Pitch, m	Pipe Diameter, m	Laps	Material Temperature, °C	Heat Transfer Temperature Difference, °C
After optimization	Feeding section	1	0.08	0.055	12	28	24
	Middle section	3	0.1	0.05	29	60	8
	Discharge section	1.5	0.12	0.05	12	67	15
Traditional equal pitch	Feeding section	1	0.1	0.05	9	25	30
	Middle section	3	0.1	0.05	27	60	5
	Discharge section	1.5	0.1	0.05	13	69	14

The basis for determining the material temperature is as follows. The feed section—handling high-moisture raw materials—adopts an initial temperature of 30 °C; the middle section, serving as the core drying zone, operates at 52 °C; and the discharge section—conveying low-moisture finished product—is maintained at 65 °C to prevent thermal denaturation of proteins. For comparison, the temperature field of a conventional constant-pitch coiled tube ranges from 25.1 °C to 72.3 °C, and its average value (55 °C) aligns well with the actual operating conditions of the equipment.

2.3.3. Optimized Three-Stage Coil Heat Transfer Power Calculation

Feeding section (0–1 m)

Single-turn helix expanded length: $L_0 = \sqrt{\left(0.08^2 + (\pi \times 0.5)^2\right)} \approx 1.573$ m;

Heat transfer area: $A_{a1} = \pi \times 0.055 \times 12 \times 1.573 \approx 3.25$ m^2;

Heat transfer power: $Q_{a1} = 800 \times 3.25 \times 24 = 62.4$ kW;

Middle section (1–4 m)

Single-turn helix expanded length: $L_0 = \sqrt{\left(0.10^2 + (\pi \times 0.5)^2\right)} \approx 1.574$ m;

Heat transfer area: $A_{a2} = \pi \times 0.050 \times 29 \times 1.574 \approx 7.16$ m^2;

Heat transfer power: $Q_{a2} = 800 \times 7.16 \times 8 = 45.824$ kW;

Discharge section (4–5.5 m)

Single-turn helix expanded length: $L_0 = \sqrt{\left(0.12^2 + (\pi \times 0.5)^2\right)} \approx 1.575$ m;

Heat transfer area: $A_{a3} = \pi \times 0.050 \times 12 \times 1.575 \approx 2.97$ m^2;

Heat transfer power: $Q_{a3} = 800 \times 2.97 \times 15 = 35.64$ kW;

Overall heat transfer performance

Total heat transfer area: $A_a = A_{a1} + A_{a2} + A_{a3} = 13.38$ m^2;

Total heat transfer power: $Q_a = Q_{a1} + Q_{a2} + Q_{a3} = 143.864$ kW;

2.3.4. Calculation of Heat Transfer Power for Traditional Constant-Pitch Coil Tubes

The total number of turns of the traditional constant-pitch coil is 49, and the unfolded length of a single turn is 1.574 m. The heat transfer area and power are calculated as follows:

Feeding section (0–1 m)
Heat transfer area: $A_{b1} = \pi \times 0.05 \times 9 \times 1.574 \approx 2.22\ m^2$;
Heat transfer power: $Q_{b1} = 800 \times 2.22 \times 30 = 53.28k\ W$;
Middle section (1–4 m)
Heat transfer area: $A_{b2} = \pi \times 0.050 \times 29 \times 1.574 \approx 6.66\ m^2$;
Heat transfer power: $Q_{b2} = 800 \times 6.66 \times 5 = 26.64\ kW$;
Discharge section (4–5.5 m)
Heat transfer area: $A_{b3} = \pi \times 0.050 \times 13 \times 1.574 \approx 3.23\ m^2$;
Heat transfer power: $Q_{b3} = 800 \times 3.23 \times 14 = 36.176\ kW$;
Overall heat transfer performance
Total heat transfer area: $A_a = A_{b1} + A_{b2} + A_{b3} = 12.11\ m^2$;
Total heat transfer power: $Q_a = Q_{b1} + Q_{b2} + Q_{b3} = 116.096\ kW$;

2.3.5. Comparison and Analysis of Heat Transfer Power

The comparison of heat transfer performance between the optimized three-segment coil and the traditional equal-pitch coil is shown in Table 3.

Table 3. Comparison of heat transfer performance of the coil before and after optimization.

Evaluation Indicators	Tradition	After Optimization	Range of Variation
Total heat transfer area, m^2	12.11	13.38	+10.5%
Total heat transfer power, kW	116.096	143.866	+23.9%
Feeding section power, kW	53.28	62.4	+17.1%
Intermediate section power, kW	26.64	45.824	+72%
Power of discharge section, kW	36.176	35.64	−1.5%

The calculation results show that the three-stage differentiated coil achieved the optimized effects of feed intensification, intermediate matching, and outlet temperature control.

In the feed section, after optimization, the material temperature reached 28 °C; the heat transfer temperature difference increased, and the heating power rose by 17.1%, thereby accelerating the heating and vaporization of high-moisture fish meal and alleviating the feed drying lag commonly observed in traditional equipment.

In the intermediate section, the material temperature remained at 60 °C for both configurations, and after optimization, the heating power increased significantly by 72%, markedly enhancing heat transfer efficiency in the core drying zone and improving overall drying stability.

In the outlet section, the moisture content of the discharged fish meal was reduced to 10–15%, falling within the protein heat-sensitive range of 60–80 °C. The traditional coil yielded an outlet temperature of 69 °C, being prone to localized heat accumulation and leading to coking and protein denaturation. In contrast, the optimized design achieved an outlet temperature of 67 °C with a slight 1.5% reduction in heating power, effectively mitigating heat accumulation and suppressing both coking and nutritional degradation.

3. Static Structural Analysis of the Spiral Heating Coil

As the core load-bearing and heat transfer component of the equipment, the spiral heating coil needs to withstand its own weight and the weight load of external fish meal materials during operation. The structural stiffness and strength of the coil directly determine the long-term operational reliability of the equipment. To accurately quantify the force and deformation characteristics of the coil [20], this study utilized the Solid Mechanics module of COMSOL 6.4 to conduct three-dimensional static simulation analysis, verifying

the structural reliability of the optimized segmented coil and providing theoretical support for the rationality of the structural design.

3.1. Equilibrium Control Equations and Modeling

The static structural simulation follows the classic assumptions of continuum mechanics. All governing equations were derived from the fundamental theory of spatial problems in elasticity [21]. The core assumptions were as follows:

- Material properties: The 304 stainless steel was modeled as an isotropic, linear elastic material with no plastic deformation, creep, or initial defects;
- Deformation state: Structural deformations were small; displacements were much smaller than the geometric dimensions of the structure, and strains remained $\leq$1%;
- Load conditions: The system was subjected to steady-state static loading only, with no acceleration, impact loads, or dynamic excitation;
- Medium characteristics: The coil was treated as a continuous solid medium, satisfying the applicability conditions of the fundamental equations of elasticity.

(1) Momentum conservation equation: Under steady-state static conditions, the acceleration $a = 0$ of the coil's micro-element was zero, and the net external force vanished. The forces acting on the micro-element comprised surface tractions (represented by the Cauchy stress tensor σ) and body forces f (in this study, solely gravity). Applying the Gauss divergence theorem to convert the surface integral of tractions into a volume integral—and subsequently dividing through by the micro-element volume—yielded the spatial static equilibrium governing equation

$$\nabla \cdot \sigma + \mathrm{f} = 0 \tag{6}$$

In this equation, σ denotes the Cauchy stress tensor, which quantifies the internal force per unit area acting on a material micro-element; $\nabla \cdot \sigma$ is the divergence of the stress tensor, representing the net internal force flux per unit volume; f is the body force vector per unit volume (in this study, $f = \rho g$); ρ is the density of the 304 stainless steel ($\rho = 7930$ kg/m^3); and g is the gravitational acceleration vector ($g = 9.81$ m/s^2).

(2) Linear elastic constitutive equation: The one-dimensional Hooke's law, $\sigma = E\varepsilon$, was extended to three-dimensional space. Both the stress tensor σ and the strain tensor ε are second-order tensors, and their linear relationship is governed by the fourth-order elastic stiffness tensor C, yielding the three-dimensional linear elastic constitutive equation

$$\sigma = E\varepsilon \tag{7}$$

In engineering applications, the elastic stiffness tensor of 304 stainless steel is uniquely determined by the Young's modulus E and Poisson's ratio ν, and its simplified isotropic form is given below [22]:

$$\sigma_{ij} = \frac{E}{1+\nu}\varepsilon_{ij} + \frac{E\nu}{(1+\nu)(1-2\nu)}\varepsilon_{kk}\delta_{ij} \tag{8}$$

In this equation, E denotes the Young's modulus, $E = 193$ GPa; ν denotes Poisson's ratio, $\nu = 0.3$; δ_{ij} is the Kronecker delta, equal to one if $i = j$ and zero otherwise; and ε_{kk} is the volumetric strain, defined as $\varepsilon_{kk} = \varepsilon_{xx} + \varepsilon_{yy} + \varepsilon_{zz}$.

(3) Geometric strain displacement equation: Under the assumption of small deformation, to ensure the symmetry of shear strain (shear strain $\varepsilon_{ij} = \varepsilon_{ji}$), strain is defined by

the symmetric part of the displacement gradient. Let the displacement vector of the infinitesimal element be

$$u = \left(u_x,\ u_y u_z\right)^T \tag{9}$$

The displacement gradient $\nabla \boldsymbol{u}$ is a second-order tensor, with components quantifying the spatial rate of change of the displacement field in each coordinate direction. To ensure the strain tensor ε satisfies major symmetry ($\varepsilon_{ij} = \varepsilon_{ji}$)—a fundamental requirement for infinitesimal strain theory—the symmetric part of $\nabla \boldsymbol{u}$ is taken, yielding the kinematic definition.

Then, the geometric relationship between strain and displacement is

$$\varepsilon = \frac{1}{2}\left(\nabla \boldsymbol{u} + (\nabla \boldsymbol{u})^T\right) \tag{10}$$

In this equation, ε denotes the strain tensor; u denotes the displacement vector; and $\nabla \boldsymbol{u}$ denotes the displacement gradient tensor, which characterizes the spatial rate of change of displacement.

3.2. Geometric Models and Material Properties

A full-scale (1:1) three-dimensional geometric model of the heating coil was constructed, with a nominal diameter of 0.5 m and total axial length of 5.5 m. The coil was modeled as 304 stainless steel and assigned the following temperature-independent room temperature mechanical properties: mass density $\rho = 7930$ kg/m^3, Young's modulus $E = 193$ GPa, and Poisson's ratio $\nu = 0.3$.

3.3. Grid Distribution Design and Independence Verification

The mesh resolution directly affects the computational efficiency and result reliability of finite element simulations. For the complex geometry of the spiral coil, a free tetrahedral mesh was generated, where the base region element size was 20 mm and key regions—including the coil wall and the heat transfer interface between the fluid and the coil—were refined to 5 mm to balance accuracy and computational efficiency. Figure 7 shows the mesh.

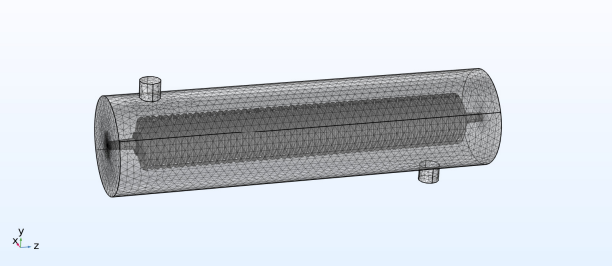


Figure 7. Meshing diagram.

To eliminate the influence of the mesh size on the numerical results, a grid independence study was performed [23], in which four meshes with progressively refined resolutions were tested comparatively. The results are presented in Table 4.

The verification results show that when the mesh contained 800,000 elements, the relative error in the predicted maximum temperature—compared with the refined 1,020,000-element mesh—was only 0.3%, satisfying the accuracy requirements for engineering simulations. Meanwhile, the computational time for the 800,000-element mesh was 3.5 h, substantially less than the 5.8 h required for the 1,020,000-element mesh. Consequently, the 800,000-element mesh was adopted for all subsequent analyses. This mesh

resolution is also suitable for coupled thermal–stress and fatigue simulations [24], ensuring consistency across multi-physics results.

Table 4. Grid independence verification.

Grid Group Number	Number of Grid Cells	Maximum Temperature Calculation Value (°C)	Relative Error (%) Compared with the Previous Group	Single-Condition Calculation Time (h)
1	423,562	76.6	-	1.2
2	612,894	78.7	2.7	2.1
3	801,247	79.1	0.5	3.5
4	1,023,561	79.3	0.25	5.8

3.4. Boundary Conditions

Boundary conditions were rigorously prescribed to replicate actual operational conditions:

(1) Displacement constraints: Both ends of the coil were fully clamped, consistent with its rigid mounting configuration in service.

(2) Body force: A uniform gravitational acceleration of 9.81 m/s^2 was applied in the negative y direction, accounting for the self-weight of the 304 stainless steel coil and the enclosed fish meal material.

(3) Surface traction: Pressure loads representing bulk material loading were applied to the coil's outer cylindrical surface. Under the full-load condition—corresponding to a total fish meal mass of 5000 kg—the resulting nominal pressure was 12.5 kPa, which was uniformly distributed over the loaded surface area.

3.5. Displacement Field Distribution and Stiffness Verification

Through numerical simulations, the displacement field distribution of the coil under various operating conditions was obtained. Owing to fixed boundary constraints at both ends, the displacement was zero, and the dominant deformation mode was vertical bending. The corresponding data are presented in Table 5.

Table 5. Displacement values at different weights.

Operating Condition Number	Weight of Incoming Materials (kg)	Maximum Displacement (mm)	Design Limit (mm)	Compliance
1—Empty material condition	0	0	1	Qualified
2—Half-year operation condition	2000	0.03	1	Qualified
3—Full load condition	4000	0.06	1	Qualified
4—Overload conditions	5000	0.075	1	Qualified

The formula for calculating the structural stiffness is

$$K = \frac{F}{\delta} \tag{11}$$

In this formula, K denotes the structural stiffness; F denotes the applied load; and δ denotes the displacement. Substituting the displacements before and after optimization under the full-load condition—0.09 mm and 0.06 mm, respectively—yields

$$\frac{K_1}{K_2} = \frac{\delta_2}{\delta_1} = \frac{0.09}{0.06} = 1.5 \tag{12}$$

The calculations show that following optimization, the stiffness of the heating coil increased by 50%, and the maximum displacement under full-load conditions was 0.06 mm, well below the industry design limit of 1.0 mm. Even under a 20% overload condition,

the displacement remained within acceptable limits, demonstrating sufficient structural overload capacity. Figure 8 shows the displacement field distribution (contour plots) of the heating coil under various load conditions, and Figure 9 presents the axial displacement comparison curves for the same conditions.

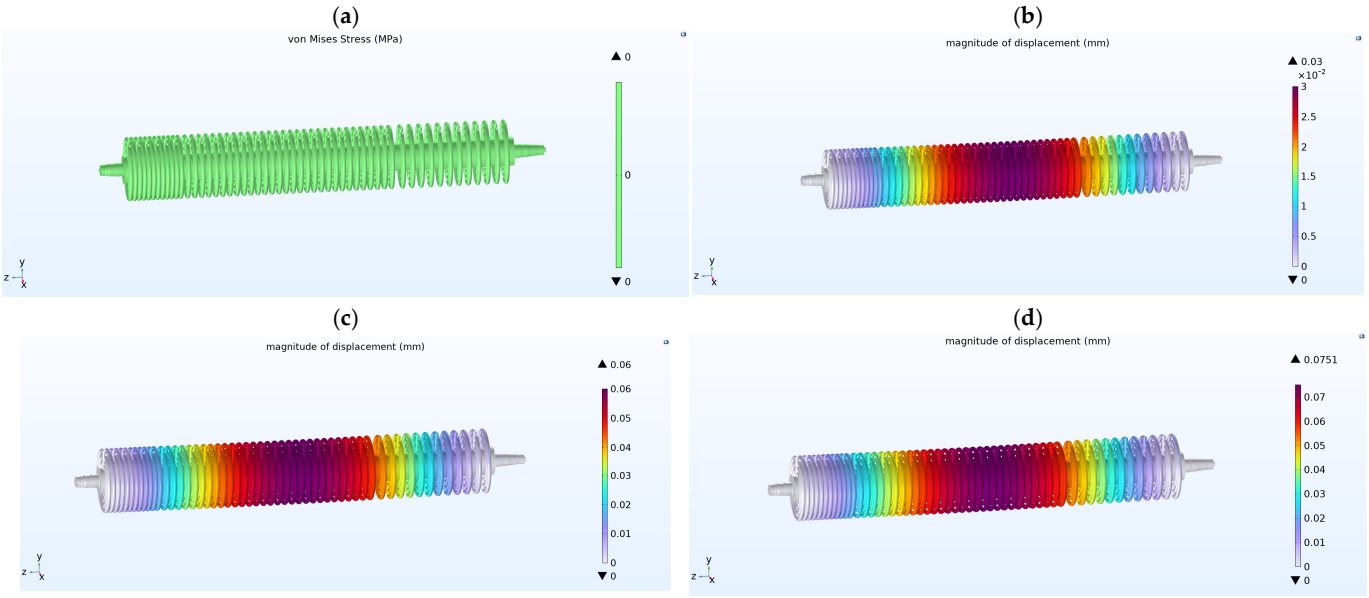


Figure 8. Contour plot of displacement field distribution of heating coils under different loading conditions. (Among them, (**a**) represents no load, (**b**) represents a load of 2 tons, (**c**) represents a load of 4 tons, and (**d**) represents a load of 5 tons).

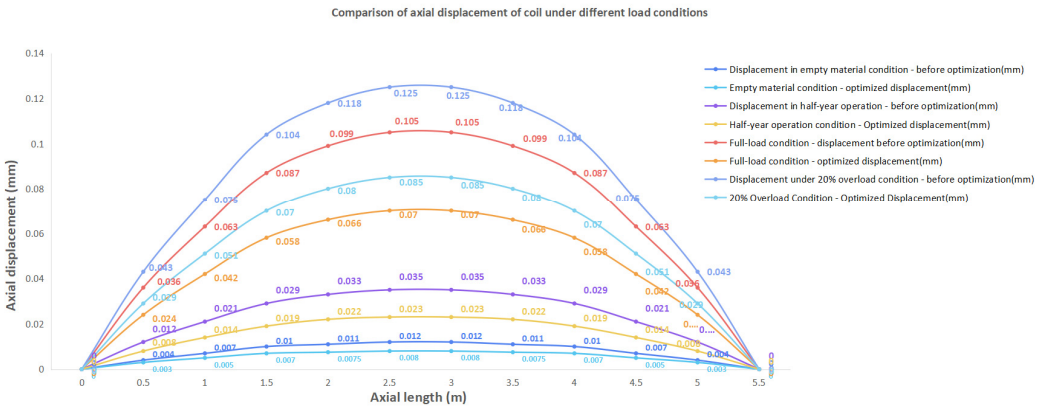


Figure 9. Comparison of axial displacement of coil under different load conditions.

The displacement distribution conformed to the mechanical behavior of a simply supported beam. The maximum displacement occurred at the axial midpoint (from 2.5 m to 3.0 m), while displacement at both ends was zero, fully consistent with the theoretical predictions. Following optimization, the axial displacement distribution became more uniform, with no pronounced local deformation, thereby effectively mitigating the failure modes observed in conventional designs, including fracture of the main shaft's inner tube and coil pipe leakage induced by excessive localized strain.

3.6. Stress Field Distribution and Structural Strength Assessment

Based on the displacement field, this study further analyzed the stress field distribution in the coil. The von Mises yield criterion—a widely accepted standard for strength assessment of ductile materials—was applied, and the allowable static stress of 304 stainless steel at ambient temperature, $[\sigma] = 130$ MPa, was determined per GB/T 150.1–2024,

"Pressure Vessels—Part 1: General Requirements [25]." The maximum static stress in the coil under various operating conditions is presented in Table 6.

Table 6. Stress values at different weights.

Operating Condition Number	Weight of Incoming Materials (kg)	Maximum Stress (MPa)	Allowable Stress (MPa)	Compliance
1—Empty material condition	0	0	130	-
2—Half-year operation condition	2000	7.87	130	16.52
3—Full load condition	4000	15.7	130	8.28
4—Overload conditions	5000	19.7	130	6.6

We define the formula for calculating the strength improvement ratio as follows:

$$r = \frac{\sigma_{1max} - \sigma_{2max}}{\sigma_{1max}} \times 100\% \quad (13)$$

In the formula, $\sigma_{1\max}$ denotes the maximum stress under full load conditions prior to optimization ($\sigma_{1\max} = 26.3$ MPa); $\sigma_{2\max}$ denotes the maximum stress under full load conditions after optimization ($\sigma_{2\max} = 15.7$ MPa); and r represents the strength improvement ratio. Substituting the values yields $r = (26.3 - 15.7)/26.3 \times 100\% = 40.3\%$. Following optimization, the coil's maximum stress was reduced by 40.3%.

The safety factor calculation is

$$n = \frac{[\sigma]}{\sigma_{max}} \quad (14)$$

Substituting the values yielded $n_1 = \frac{[\sigma]}{\sigma_{1max}} = \frac{130}{26.3} = 4.94$ and $n_2 = \frac{[\sigma]}{\sigma_{2max}} = \frac{130}{15.7} = 8.28$. The safety factor increased from 4.94 to 8.28, fully satisfying the strength requirements for long-term operation. Figure 10 presents the stress field distribution contour plots of the heating coil under various load conditions.

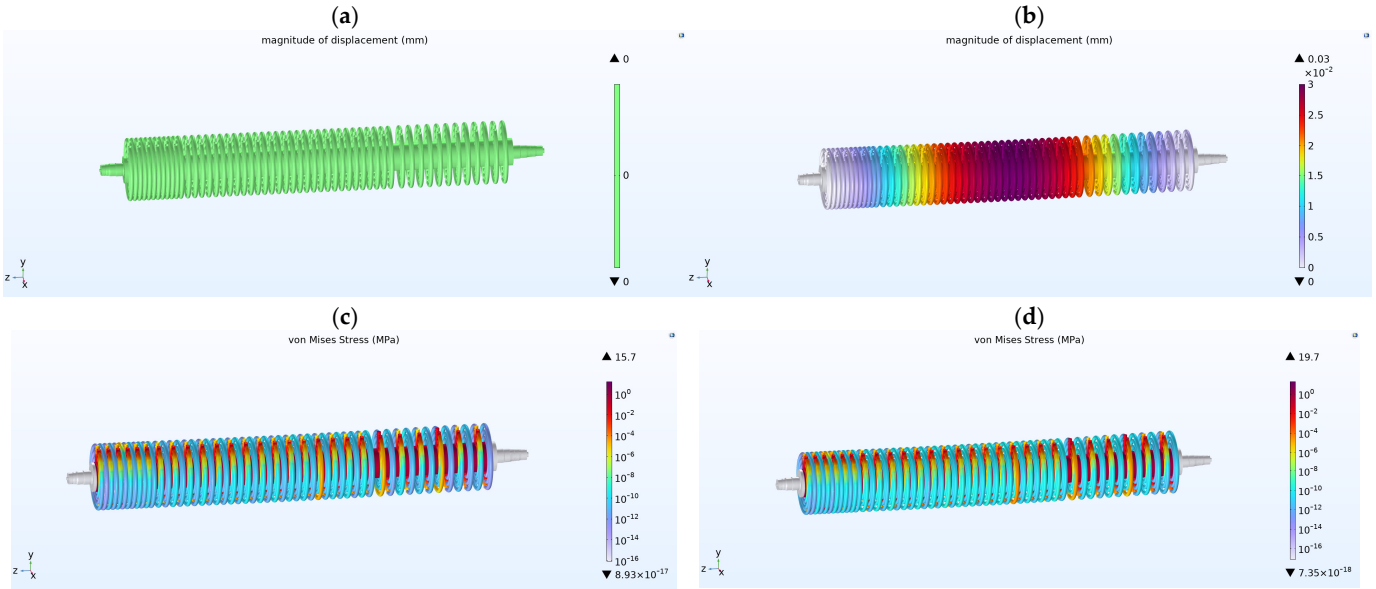


Figure 10. Stress field distribution contour map of heating coil under different loading conditions. (Among them, (**a**) represents no load, (**b**) represents a load of 2 tons, (**c**) represents a load of 4 tons, and (**d**) represents a load of 5 tons).

Figure 11 presents the axial displacement comparison curves of the coil under various load conditions.

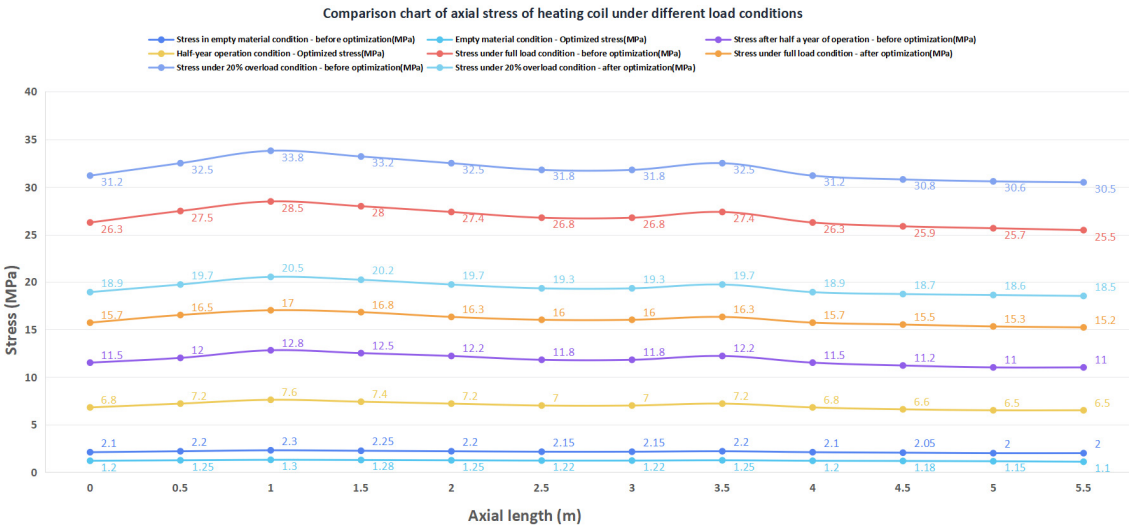


Figure 11. Comparison chart of axial stress of heating coil under different load conditions.

As shown in Figure 11, the axial stress distribution became more uniform after optimization, with no discernible stress concentration zones. The optimization effectively eliminated stress peaks at critical locations—such as welds and shaft-head connections—in the conventional structure, thereby significantly reducing the risk of fatigue cracking. This satisfies the equipment's long-term operational strength requirements.

4. Thermal Simulation Analysis of Spiral Heating Coil

To quantitatively verify the heat transfer uniformity, thermal stress level, and long-term thermal fatigue reliability of the optimized three-segment heating coil, this section established a fully coupled heat transfer model—incorporating solid conduction, porous medium heat transfer, surface radiation, and phase-change latent heat—using the COMSOL Multiphysics® 6.4 platform. Steady-state thermal simulations, thermal–structural sequential coupling analyses, and thermal fatigue life assessments were performed for both the conventional constant-pitch coil and the optimized segmented coil. The optimization effect was rigorously validated across the three core metrics: temperature field distribution, thermal stress magnitude, and thermal fatigue life.

4.1. Comparative Analysis of Temperature Field Distribution

The thermal simulation modeling in this section followed the classical theories of heat transfer and the fundamental assumptions of heat transfer in porous media. All governing equations were derived from heat transfer fundamentals [26], porous medium heat transfer theory [27], and the standard radiative heat transfer model for vacuum environments. The core assumptions were as follows:

− Convection heat transfer in the vacuum chamber was negligible; only conduction, radiation, and phase-change heat transfer occurred.
− Fish meal was modeled as a uniform, isotropic porous medium satisfying the equivalent continuum theory.
− The heating steam flowed under steady-state conditions, and heat conduction through the pipe wall was governed by steady-state conduction.
− The chamber insulation layer remained intact, with zero heat loss from the outer surface; thus, the outer boundary was treated as adiabatic.

4.1.1. Governing Equation for Heat Transfer

The drying heat transfer process in a vacuum environment is a complex process involving coupling of multiple mechanisms. It mainly includes convective heat transfer of the heating medium in the coil, heat conduction through the coil wall, heat conduction and phase change heat transfer within the porous medium of fish meal, and surface radiation heat transfer in the storage bin. The core control equations are as follows:

(1) Energy conservation equation for solid regions: Based on the first law of thermodynamics (the principle of energy conservation) and Fourier's law of heat conduction, the net rate of heat transfer into a differential element in a steady-state, source-free, and macroscopically stationary solid region is zero, ensuring local thermal equilibrium. This yields the governing equation when combined with Fourier's law:

$$q = -k\nabla \mathrm{T} \tag{15}$$

Based on the principle of energy conservation and the Gauss divergence theorem, the heat flux term was converted from a surface integral to a volume integral. Upon cancellation of the infinitesimal volume element, the steady-state energy conservation equation for a solid medium was derived:

$$\nabla \cdot (k\nabla \mathrm{T}) = 0 \tag{16}$$

In this equation, k represents the thermal conductivity of the solid material; T is the temperature field in the solid region; ∇T is the temperature gradient; and q is the heat flux density vector.

(2) Equivalent heat transfer model for porous media: Fish meal was modeled as a solid–gas two-phase porous medium. The equivalent thermal conductivity was computed using the volume-weighted averaging method, where the total conductive heat flux equaled the sum of the contributions from the solid matrix and the pore gas. The resulting expression for the equivalent thermal conductivity is

$$k_{eff} = \varepsilon k_f + (1 - \varepsilon) k_s \tag{17}$$

In this formula, k_{eff} denotes the effective thermal conductivity of the fish meal porous medium; ε is the porosity of the fish meal, set to 0.4 in this study; k_f is the thermal conductivity of the rarefied gas in the pores, taken as 0.026 W/(m·°C); and k_s is the thermal conductivity of the solid matrix of the fish meal, taken as 0.18 W/(m·°C). Substituting these values yields k_{eff} = 0.12 W/(m·°C), consistent with the experimentally measured value.

(3) Latent heat source term: Based on the phase-change heat transfer theory for water evaporation, latent heat was absorbed during liquid water evaporation in the fish meal drying process and modeled as a negative volumetric heat source term in the energy equation [28]. The expression for the latent heat absorption rate per unit volume is

$$Q = \rho_l H_{lv} \frac{\partial_{\alpha l}}{\partial_t} \tag{18}$$

In this formula, Q denotes the volumetric latent heat source term; ρ_l is the density of liquid water, taken as 1000 kg/m^3; H_{lv} is the latent heat of vaporization of water, taken as 2260 kJ/kg; αl is the volume fraction of liquid water; and $\partial_{\alpha l}/\partial_t$ is the time derivative of the liquid water volume fraction.

(4) Radiative heat transfer equation: Based on the Stefan–Boltzmann law and the surface-to-surface (S2S) radiation model, radiative heat exchange between the silo wall and the material dominated in vacuum conditions where convective heat transfer was absent. The net radiative heat flux density at a gray diffuse surface is

$$q_r = \varepsilon\sigma\left(T_{sur}^4 - T^4\right) \quad (19)$$

In this formula, q_r denotes the net radiative heat flux density; ε is the surface emissivity, set to 0.85 for both the fish meal and the silo wall; σ is the Stefan–Boltzmann constant, taken as 5.67×10^{-8} W/(m^2·K^4); T_{sur} is the temperature of the silo wall; and T is the surface temperature of the material.

4.1.2. Material Properties

The material property parameters used in the simulation were all standard industrial parameters, as detailed in Table 7:

Table 7. Material property parameters for simulation.

Material Type	Density ρ (kg/m^3)	Constant Pressure Specific Heat Capacity c_P (J/(kg·°C))	Thermal Conductivity k (W/(m·°C))	Surface Emissivity ε
304 stainless steel	7930	500	16.2	0.35
Fish meal porous medium	650	2100	0.12	0.90
Heating medium (steam)	600	2043	0.025	-

4.1.3. Boundary Conditions and Numerical Solution Configuration

The boundary conditions and solution settings conformed to actual operating conditions:

(1) Coil inlet: The heating inlet temperature was set to 70 °C, and the flow velocity was 0.8 m/s; the convective heat transfer coefficient h inside the tube was calculated using the Dittus–Boelter correlation:

$$N_u = 0.023 Re^{0.8} Pr^{0.4} \quad (20)$$

Here, N_u is the Nusselt number, Re is the Reynolds number, and Pr is the Prandtl number. h = 3200 W/(m^2·°C).

(2) Outer wall of the warehouse: A 0-mm-thick silica–alumina insulation layer was used, modeled as an adiabatic boundary (heat flux density = 0);

(3) Initial conditions: The model's initial temperature was 25 °C;

(4) Solver: A steady-state solver with a relative residual convergence criterion of 1×10^{-6} was used.

4.1.4. Comparative Analysis of Simulated Temperature Distributions

The traditional constant-pitch heating coil employs a uniform pitch and constant pipe diameter. During the initial drying stage, when the moisture content of fish meal is 60–70%, substantial heat input is required to drive water vaporization; however, insufficient heat transfer capacity in the feed zone results in a slow material temperature rise. In the later drying stage, the moisture content decreases significantly, and excessive heat supply in the discharge zone then causes localized overheating, inducing protein denaturation and coking (Figure 12). This configuration exhibits a temperature distribution ranging from 25.1 to 72.3 °C, with an axial temperature gradient of 8.6 °C/m, clearly indicating inadequate heating at the feed zone and excessive temperatures at the discharge zone. The optimized

segmented coil directly addresses these limitations. As shown in Figure 13, it yielded a more uniform temperature field, with a temperature range of 33.2–67.2 °C and a reduced axial temperature gradient of 6.2 °C/m, thereby precisely satisfying the phase-dependent heat transfer requirements of fish meal drying.

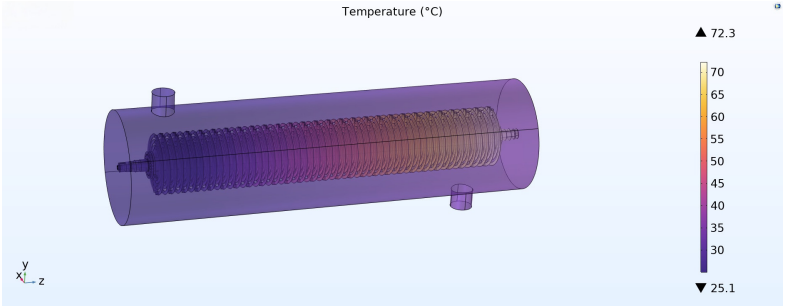


Figure 12. Temperature field distribution contour map of traditional constant-pitch heating coil.

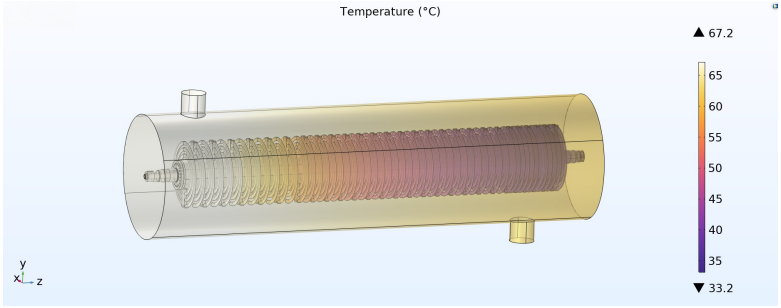


Figure 13. Temperature field distribution cloud map of the optimized heating coil.

The axial temperature distribution of the heating coil is compared in Figure 14. As shown in the figure, no significant local overheating occurred along the entire axial length, resolving the fish meal coking and protein denaturation caused by excessive discharge-end temperatures in the traditional configuration.

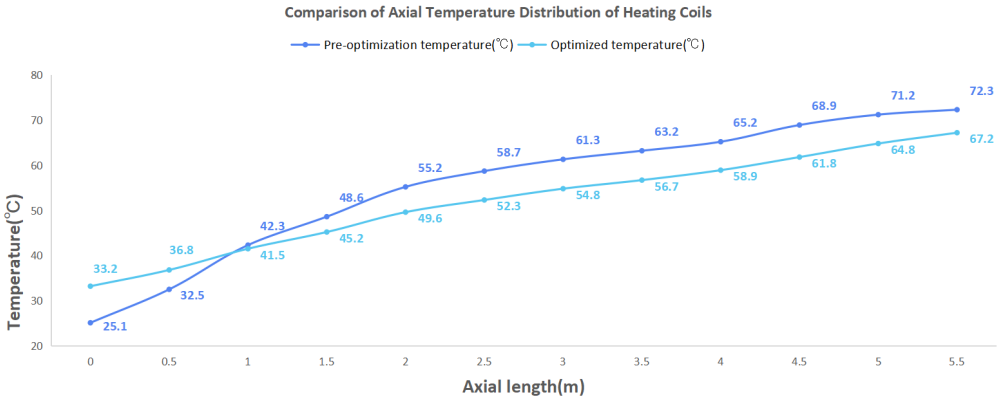


Figure 14. Comparison of axial temperature distribution of heating coils.

4.2. Thermo-Mechanical Coupled-Field Simulation

The computed temperature field distributions were imported as thermal loads into the solid mechanics module to perform sequential thermal–structural coupling analysis. This enabled quantitative comparison of the thermal deformation and thermal stress between the two coil configurations, thereby assessing their relative thermal structural stability [28].

4.2.1. Governing Equation for Thermoelastic Stress

(1) Continuity equation for linear momentum

The momentum conservation equation is consistent with the statics equation:

$$\nabla \cdot \sigma + \boldsymbol{f} = 0 \tag{21}$$

Here, σ represents the Cauchy stress tensor, and $\boldsymbol{f}$ stands for the gravitational load.

(2) Thermoelastic Constitutive Equation

The linear thermoelastic constitutive equation is

$$\sigma = C : (\varepsilon - \varepsilon_{th}) \tag{22}$$

Here, C denotes the elastic stiffness tensor; ε represents the total strain tensor; and ε_{th} denotes the thermal strain tensor. Based on the fundamental law of thermal expansion, the linear expansion of isotropic materials is linearly proportional to both the temperature change and the original length. By combining the definition of linear thermal strain—the ratio of expansion to original length—and eliminating the original length, we obtain

$$\varepsilon_{th} = \alpha\left(T - T_{ref}\right) \tag{23}$$

Here, α represents the thermal expansion coefficient of the material, T is the current temperature, and T_{ref} is the stress-free reference temperature, which was set to 25 °C.

4.2.2. Materials and Boundary Conditions for Coupled Simulation

For the 304 stainless steel coil, the material parameters for the structural simulation were as follows: elastic modulus E = 193 GPa, Poisson's ratio ν = 0.3, and thermal expansion coefficient α = 16.0 × 10^{-6}/°C, all of which are standard industrial parameters.

The boundary conditions were as follows:

(1) Displacement constraints: The two ends of the coil pipe were fixed.
(2) Temperature load: The simulation results of the mapped temperature field were used (with consistent grids to avoid interpolation errors).
(3) Gravity load: This was set to 9.81 m/s^2 in the y direction.

4.2.3. Comparison of Thermal Stress Simulation Results

Owing to the excessive axial temperature gradient, the traditional coil exhibited pronounced spatial variations in thermal expansion deformation, generating substantial thermal stress—peaking at 122 MPa, only 8 MPa below the allowable thermal stress of 304 stainless steel (130 MPa)—and thus posing a high risk of stress overload during prolonged operation. As shown in Figure 15, the maximum stress occurred at the transition zone between the mid-section and the discharge zone, where the temperature gradient was steepest and the mismatch in thermal strain was most severe, resulting in distinct local stress concentration. As illustrated in Figure 16, the optimized coil achieved effective temperature gradient control, reducing the peak thermal stress to 83.7 MPa, well within the material's allowable limit.

Figure 17 compares the axial thermal stress distributions of the heating coils. Following optimization, the thermal stress increased linearly and smoothly along the axial direction—from 58.2 MPa to 83.7 MPa—with no sharp peaks or local stress concentrations across the entire length. This yielded a markedly improved distribution uniformity and fully eliminated the thermal stress overload previously observed in the discharge zone of the traditional configuration.

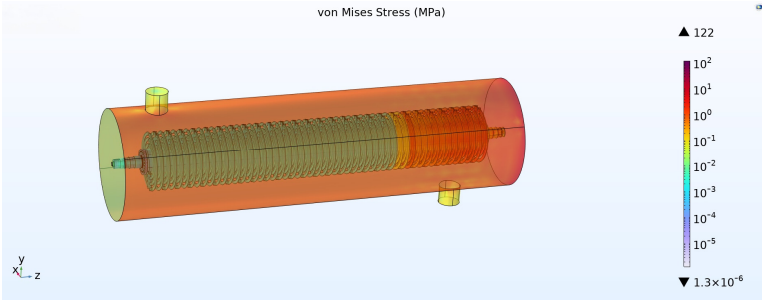


Figure 15. Contour plot of thermal stress distribution in traditional constant-pitch heating coil.

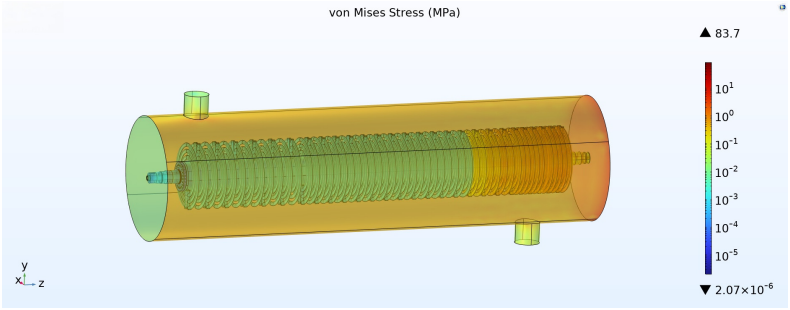


Figure 16. Schematic cloud diagram of stress field distribution for the optimized heating coil.

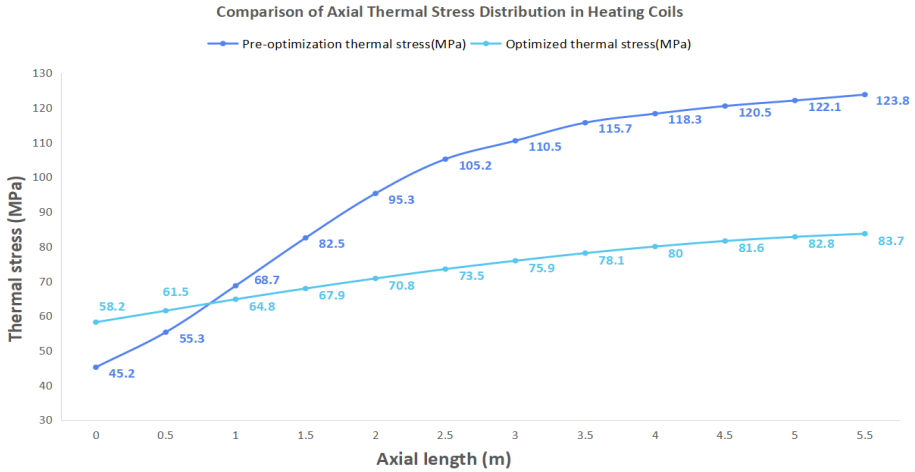


Figure 17. Comparison of axial thermal stress distribution in heating coils.

4.3. Calculation and Analysis of Thermal Fatigue Life

Thermal fatigue life of the two coil configurations was assessed using the Miner linear damage rule and the experimentally derived S–N curve for 304 stainless steel, based on computed thermal stress histories. This analysis enabled quantitative evaluation of long-term operational reliability under cyclic thermal loading.

4.3.1. Fatigue Life Calculation Model

(1) Miner's damage criterion: Derived from linear fatigue damage accumulation theory, this criterion states that material fatigue failure occurs when the cumulative damage across all stress levels reaches unity, i.e., the critical value of one, representing the threshold of fatigue failure. Consequently, the following relationship was obtained:

$$\sum_{i=1}^{n} \frac{n_i}{N_i} = 1 \quad (24)$$

In the equation, n_i denotes the number of cycles at the ith stress level, and N_i denotes the number of cycles to failure at that stress level. This criterion neglects load sequence effects on fatigue damage accumulation, offers computational simplicity, and is applicable to fatigue life estimation in conventional engineering contexts.

(2) S-N fatigue curve

In engineering practice, the power-law function form—where C and m are empirical fitting parameters—is commonly employed for fatigue life data correlation [29]:

$$S^m N = C \tag{25}$$

Among this formula, S represents the stress amplitude (MPa), and N represents the number of failure cycles.

(3) Mean Stress Correction

The Goodman correction method transforms the S–N curve for asymmetric loading into the corresponding curve for fully reversed ($R = -1$) loading, thereby eliminating the influence of the stress ratio R on fatigue life prediction. This method replaces the original "stress amplitude–mean stress" pair with its Goodman-equivalent mean stress—defined as the mean stress that, under fully reversed conditions, yields the same fatigue life—and solves for the equivalent fully reversed stress amplitude S_i [30]. The calculation formula is

$$1 = \frac{S_{ai}}{S_i} + \frac{S_{mi}}{\sigma_b} \tag{26}$$

In this equation, S_i denotes the equivalent zero-mean stress amplitude; S_{ai} denotes the ith stress amplitude; S_{mi} denotes the ith mean stress; and σ_b denotes the ultimate tensile strength.

During the operation of the vacuum dryer, a periodic temperature cycle occurs from room temperature (25 °C) to the operating temperature (70 °C). Temperature affects the coil's fatigue life in two primary ways: (1) an elevated temperature reduces the fatigue strength of 304 stainless steel—under operating conditions of 60–80 °C, the material's fatigue limit decreases by 10–15% relative to that at room temperature [31]—and (2) axial temperature gradients induce cyclic thermal stresses, which, when superimposed on mechanical loads, increase the actual stress amplitude and thereby accelerate fatigue damage [32]. To account for temperature effects, a temperature correction factor, K_T, was introduced to modify the stress amplitude:

$$K_T = \frac{\sigma_{-1}(T)}{\sigma_{-1}(25\ ^\circ\mathrm{C})} \tag{27}$$

In this equation, $\sigma_{-1}(T)$ denotes the symmetrical bending fatigue limit at the operating temperature T, and $\sigma_{-1}(25\ ^\circ\mathrm{C})$ denotes the fatigue limit at ambient temperature. Based on the optimized operating temperature range of the coil, the temperature correction factor K_T was set to 0.85, indicating a 15% reduction in the material's fatigue strength due to elevated temperature [33].

On this basis, the temperature-corrected equivalent stress amplitude was obtained:

$$S_{eq,i} = K_T \cdot S_i \tag{28}$$

We substituted $S_{eq,i}$ into the S–N curve and Miner's criterion to perform fatigue life calculations, thereby enabling the model to account simultaneously for the coupled effects of mechanical stress, mean stress, and temperature on both material properties and thermal

stress [34], a formulation more consistent with the actual fatigue failure mechanism of the equipment.

The simulation employed the COMSOL Fatigue module, integrated with the equipment's intermittent operational profile. A complete thermal cycle was defined as one production batch encompassing the temperature excursion from ambient (25 °C) to operating temperature (70 °C) and back to ambient.

4.3.2. Comparison of Fatigue Life Calculation Results

The traditional coil exhibits an axial temperature gradient of 8.6 °C/m, inducing pronounced non-uniform thermal expansion and consequently generating substantial additional thermal stress. Superimposed on mechanical loading, this elevates the stress amplitude markedly. Concurrently, localized temperatures in the discharge zone exceed 70 °C, further degrading the material's fatigue strength. Under thermomechanical cyclic coupling, the fatigue life is limited to 3220 cycles. Assuming three production batches per day, the service life is merely 2–3 years, identifying thermomechanical fatigue as the root cause of recurrent coil failure. As illustrated in Figure 18 (fatigue life distribution contour), the traditional coil showed highly non-uniform life distribution, with the transition zone constituting a critical weak region. In contrast, the optimized coil reduced the axial temperature gradient to 6.2 °C/m, yielding a more uniform temperature field and stabilizing the operational temperature across the full length at 33.2–67.2 °C, thereby minimizing fatigue strength degradation. Under identical thermomechanical cycling and loading conditions, its fatigue life extended to 12,000 cycles, supporting an industrial service life exceeding 10 years. Figure 19 confirms uniform life distribution, with the minimum life satisfying long-term operational requirements and effectively resolving the industry-wide challenge of thermal fatigue failure.

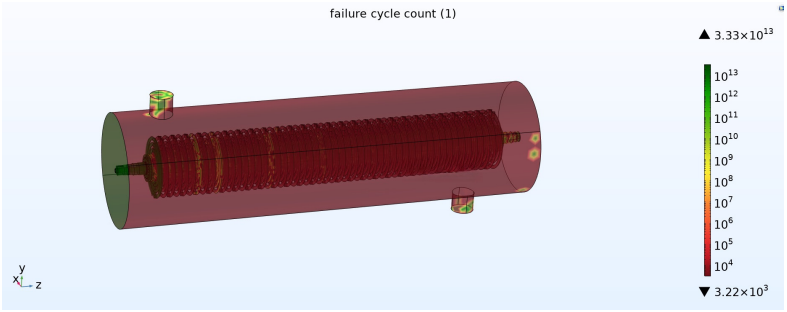


Figure 18. Fatigue life distribution contour map of traditional constant-pitch heating coil.

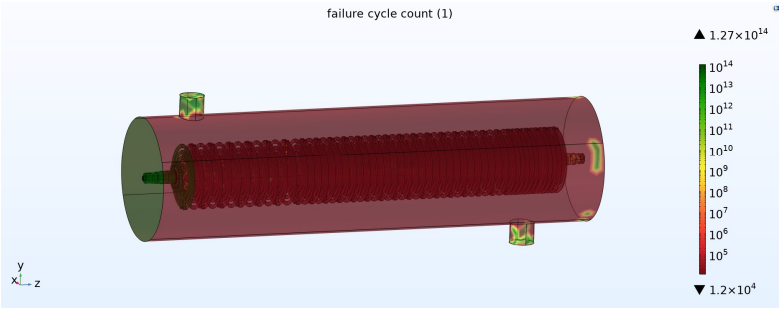


Figure 19. Fatigue life distribution contour map of optimized heating coil.

Figure 20 compares the axial fatigue life distributions of the heating coils. A thermally coupled porous media heat transfer model was developed via thermal analysis, with thermal boundary conditions refined to account for the thermophysical properties of saturated water vapor. Comparative evaluation between the traditional and optimized coil configurations

confirmed that the drying cycle was shortened effectively and fish meal coking was eliminated, thereby fully validating the engineering rationality of the proposed improvement.

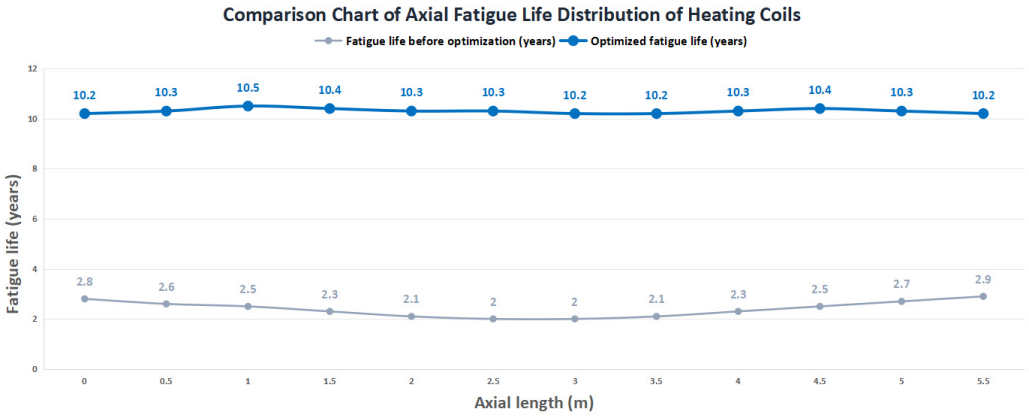


Figure 20. Comparison chart of axial fatigue life distribution of heating coils.

5. Experimental Investigation and Optimization of Process Parameters for Fish Meal Drying

5.1. Key Process Parameters and Identification Methods of Fish Meal

Drawing on industrial operational experience and preliminary experimental trials, the three principal process parameters governing the quality of vacuum-dried fish meal have been identified as the heating temperature [35], vacuum degree, and drying time [36,37]. These parameters critically influence water evaporation kinetics, protein structural stability (i.e., denaturation extent), and overall process efficiency. The moisture content and crude protein content constitute the primary quality metrics; their target specification ranges were established empirically through systematic experimentation (parameter identification methodology detailed in Table 8).

Table 8. Sensor models and measurement parameters.

Detection Parameter	Sensor Model	Measurement Range
Drying chamber temperature	PT100 platinum resistance sensor	−50∼200 °C
Vacuum degree of drying chamber	Capacitive vacuum sensor	0∼0.1 MPa
Material humidity	High-frequency capacitive humidity sensor	0∼100%
Motor speed	Incremental encoder	0∼6000 r/min
Heating tube current	Current transducer	0∼5 A

The heating temperature governs the thermal energy input. Excessively high temperatures induce irreversible protein denaturation and lipid oxidation, compromising nutritional quality, functional properties, and shelf-life stability. Conversely, insufficient temperatures prolong the drying time, reduce throughput, and increase specific energy consumption.

The vacuum degree directly determines the saturation temperature of water. An elevated vacuum degree facilitates low-temperature drying, thereby preserving protein conformation and minimizing thermal degradation. However, an excessively deep vacuum imposes higher demands on the vacuum pump capacity, system integrity, and maintenance frequency, leading to increased capital investment and operational expenditures.

The drying time controls final moisture removal. An inadequate duration results in residual moisture exceeding the industry-standard limit of ≤8.0 wt%, elevating microbiological risk and limiting storage stability. Excessive duration promotes Maillard reactions,

lysine racemization, and unnecessary thermal energy utilization, degrading product quality and diminishing energy efficiency.

5.2. Fish Meal Experiment Design

Response surface methodology (RSM) was employed to quantitatively evaluate the individual and interactive effects of multiple process variables on the response. This design enables efficient experimental coverage with uniformly distributed test points and a minimal number of runs, thereby yielding a statistically robust second-order polynomial regression model.

The independent variables were defined as the heating temperature (A), vacuum degree (B), and drying time (C). The crude protein content of fish meal served as the primary response variable, selected as the key quality metric based on its direct correlation with nutritional value and functional performance. Ranges for each factor were established through preliminary trials and critical review of the literature [38]. The heating temperature (50–80 °C) was selected to balance drying kinetics against thermal-induced protein denaturation; the vacuum degree (0.03–0.08 MPa) was optimized to achieve effective low-temperature operation while constraining system capital and operational costs; and the drying time (30–120 min) was calibrated to ensure complete moisture removal without excessive thermal exposure.

A central composite design (CCD) comprising three factors at three coded levels (−1, 0, and +1) was implemented, totaling 17 experimental runs [39], including 8 factorial points, 9 axial points, and 3 replicates at the center point (65 °C, 0.055 MPa, 75 min). The center-point replicates served two purposes: estimating the pure error and assessing the model's lack of fit. All experiments were conducted in randomized order with triplicate measurements per run. The response values represent arithmetic means, reported with a standard deviation where applicable (Table 9).

Table 9. Experimental design table for horizontal response surface analysis.

Factor	Level		
	−1	**0**	**1**
Heating temperature A (°C)	50	65	80
Vacuum degree B (MPa)	0.03	0.055	0.08
Drying time C (min)	30	75	120

5.3. Experimental Process

The experimental process was as follows: material pretreatment → equipment debugging and calibration → drying experiment operation → quality inspection and data recording → post-experiment processing and repeated experiments [40].

5.4. Experimental Data Recording

Cod meal was selected as the representative feedstock for this experimental study. All reported data in Table 10 correspond to the arithmetic means of three independent replicate trials, with standard deviations provided where statistically meaningful.

Table 10. Cod material response surface experimental data.

Experiment No.	Heating Temperature A (°C)	Vacuum Degree B (MPa)	Drying Time C (min)	Protein Content (%)
1	50	0.03	75	60.2
2	80	0.055	30	62.5

Table 10. *Cont.*

Experiment No.	Heating Temperature A (°C)	Vacuum Degree B (MPa)	Drying Time C (min)	Protein Content (%)
3	65	0.03	120	60.8
4	65	0.055	75	64.2
5	80	0.055	120	63.2
6	65	0.055	75	64.1
7	65	0.055	75	64
8	65	0.08	30	63.1
9	50	0.08	75	63.8
10	80	0.08	75	63.7
11	65	0.055	75	63.8
12	80	0.03	75	61.1
13	50	0.055	30	62.3
14	65	0.08	120	63.8
15	65	0.055	75	63.9
16	50	0.055	120	62.3
17	65	0.03	30	60.5

5.5. Experimental Findings and Discussion

5.5.1. Analysis of Drying Kinetics Characteristics

Experimental data obtained from cod meal were imported into Design-Expert 13.0 software (Stat-Ease, Inc., Minneapolis, MN, USA) for response surface methodology (RSM) modeling [41]. The heating temperature (A), vacuum degree (B), and drying time (C) were designated as independent variables, while the crude protein content served as the quantitative response variable. A full quadratic model was initially fitted; non-significant terms ($p > 0.05$) were sequentially removed via backward stepwise regression to yield a statistically parsimonious and predictive final model [42]:

$$Y_{\text{cod}} = 38.83 + 0.4 \times A + 300.267 \times B + 0.041 \times C - 0.67 \times AB + 0.00026 \times AC + 0.09 \times BC - 0.0028 \times A^2 - 1860 \times B^2 - 0.00039 \times C^2 \quad (29)$$

Analysis of variance (ANOVA) was performed to assess the statistical significance and adequacy of the final RSM model (Table 11). A model was considered statistically valid when the overall model's *p* value was less than 0.05 and the lack of fit was non-significant (*p* > 0.05), confirming both model reliability and experimental reproducibility. As shown in Table 7, the linear terms—A (heating temperature), B (vacuum degree), and C (drying time)—exhibited *p* values < 0.05, indicating their individual effects on the crude protein content were statistically significant. Furthermore, all quadratic terms (A^2, B^2, and C^2) yielded *p* values < 0.0001, demonstrating highly significant curvature, i.e., pronounced nonlinear (parabolic) relationships between each factor and the response.

Table 11. Regression analysis results of the codfish model and regression coefficients.

Source	Sum of Squares	Degree of Freedom	Mean Square	F Value	*p* Value	Salience
Model	29.72	9	3.30	137.99	<0.0001	extremely significant
A, heating temperature	0.4512	1	0.4512	18.86	0.0034	significant
B, vacuum degree	17.40	1	17.40	727.37	<0.0001	extremely significant
C, drying time	0.3612	1	0.3612	15.10	0.0060	significant
AB	0.2500	1	0.2500	10.45	0.0144	significant
AC	0.1225	1	0.1225	5.12	0.0581	not significant
BC	0.0400	1	0.0400	1.67	0.2371	not significant
A^2	1.71	1	1.71	71.51	<0.0001	extremely significant
B^2	5.69	1	5.69	237.80	<0.0001	extremely significant
C^2	2.61	1	2.61	109.12	<0.0001	extremely significant

Table 11. *Cont.*

Source	Sum of Squares	Degree of Freedom	Mean Square	F Value	*p* Value	Salience
Residual	0.1675	7	0.0239			
Lack-of-fit term	0.0675	3	0.0225	0.9000	0.5151	not significant
Pure error	0.1000	4	0.0250			
Total deviation	29.88	16				

Note: $p < 0.0001$ is extremely significant; $p < 0.05$ is significant.

The model diagnostic statistics (Table 12) indicated excellent predictive performance. The coefficient of variation (CV) was 0.2464% (<10%), confirming low experimental error and high model precision, and the determination coefficient $R^2 = 0.9944$ (>0.90), the adjusted $R^2_{Adj} = 0.9872$, and the predicted $R^2_{Pre} = 0.9586$ exhibited a difference of only 0.0286 (<0.20), satisfying the criterion for model robustness and cross-validated predictability. Collectively, these metrics confirm that the final RSM model is statistically sound, highly reliable, and suitable for quantitative prediction of crude protein content and subsequent process optimization [43].

Table 12. The results of the model correlation analysis in the experiment.

Project	Numerical Value	Project	Numerical Value
Standard deviation	0.1547	Coefficient of determination (R^2)	0.9944
Mean	62.78	Adjusted coefficient of determination (R^2_{Adj})	0.9872
Coefficient of variation C.V. %	0.2464	Predictive determination coefficient (R^2_{Pre})	0.9586
		Accuracy Adeq precision	31.7134

The relative significance of the individual factors—based on their standardized regression coefficients and corresponding **p** values—was ranked as follows: vacuum degree (B) > drying time (C) > heating temperature (A).

5.5.2. The Influencing Laws of Each Factor on Drying Quality and Their Interaction Effects

Regarding the effect of the heating temperature on the crude protein content (Figure 21a), a unimodal response was observed over the range of 50–80 °C, with the peak content attained at 65 °C (64.2 wt%). From 50 to 65 °C, elevated temperatures accelerated moisture removal, thereby reducing the thermal exposure time and minimizing irreversible protein denaturation; consequently, protein concentration increased progressively. Above 65 °C, excessive thermal energy disrupted secondary and tertiary protein structures while concurrently promoting lipid peroxidation, with both mechanisms contributing to measurable protein loss. Thus, 65 °C represents the thermally optimal setpoint for preserving protein integrity.

For the effect of the vacuum degree on the crude protein content (Figure 21b), the protein content increased monotonically from 60.2 wt% to 64.2 wt% (a relative gain of 6.6%) as the vacuum degree rose from 0.03 to 0.08 MPa. This improvement is attributable to the depression of water's boiling point, enabling effective moisture removal at lower bulk temperatures and enhanced vapor mass transfer that limited oxidative degradation by reducing the oxygen residence time within the drying chamber. Beyond 0.08 MPa, marginal gains in protein content (<0.5 wt%) were outweighed by disproportionate increases in energy demand and operational complexity for vacuum maintenance; therefore, 0.08 MPa was established as the economically and technically justified upper bound.

For the effect of the drying time on the crude protein content (Figure 21c), over 30–120 min, the protein content exhibited an initial plateau followed by a gradual decline after 75 min. During the first 75 min, progressive moisture reduction elevated the apparent protein concentration without inducing significant structural damage, indicating operation

below the kinetic threshold for thermal denaturation. Beyond 75 min, the material reached moisture equilibrium (final water activity <0.2), and further drying induced cumulative conformational changes in the proteins and unnecessary energy expenditure, resulting in a slow but measurable decrease in recoverable protein. Hence, 75 min was identified as the time-optimal endpoint for maximizing protein retention.

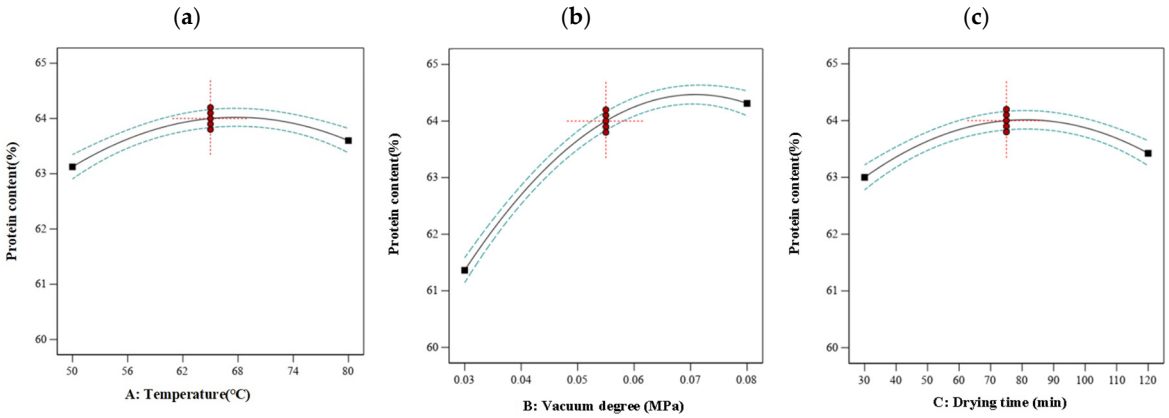


Figure 21. Trend chart of protein content for a single factor: (**a**) temperature; (**b**) vacuum degree; and (**c**) drying time.

In the interaction effect analysis, the heating temperature × vacuum degree interaction exhibited pronounced statistical significance (*p* < 0.001; Figure 22a), as evidenced by a steeply inclined response surface and elliptical, asymmetric contours, indicative of strong synergistic nonlinearity rather than additive effects. Under a low vacuum degree (0.03 MPa), thermal sensitivity was heightened; protein denaturation accelerates markedly above 60 °C, necessitating strict temperature control. Conversely, at a high vacuum degree (0.08 MPa), the depressed boiling point permitted safe operation up to 70 °C while sustaining >95% protein retention, demonstrating vacuum-mediated thermal buffering. The temperature × drying time interaction was moderate (*p* = 0.024; Figure 22b); elevated temperatures required proportionally shorter exposure times to avoid cumulative denaturation, whereas lower temperatures allowed extended durations without compromising structural integrity, thus enabling flexible trade-offs between throughput and quality, fully consistent with the univariate optima identified earlier.

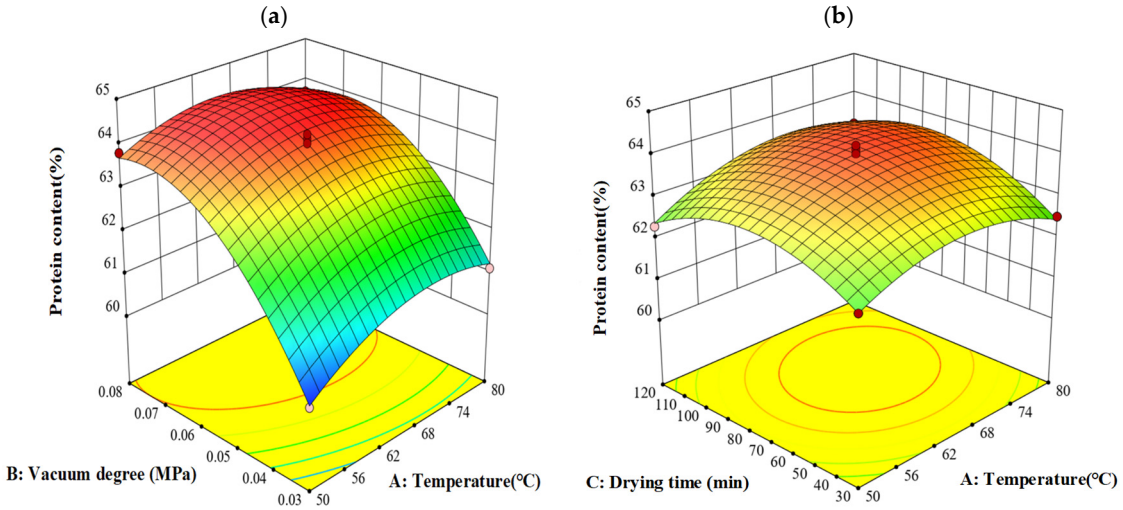


Figure 22. Interaction effects: (**a**) temperature–vacuum degree and (**b**) temperature–drying time.

Response surface modeling and experimental validation jointly identified the globally optimal drying parameters for cod meal as follows: heating temperature = 65 °C, vacuum degree = 0.08 MPa, and drying time = 75 min. This combination established a thermodynamically favorable microenvironment—characterized by reduced thermal load, minimized oxygen partial pressure, and enhanced mass transfer—thereby suppressing both conformational protein denaturation and lipid peroxidation at their mechanistic origins.

5.6. Performance Comparison Between the Optimized Equipment and the Traditional Equipment

A comparative performance evaluation was conducted between the optimized vacuum low-temperature drying process and the conventional hot air drying process, using cod meal as the test material under identical throughput conditions (150 kg/h). Key evaluation metrics included operational parameters, product quality attributes (crude protein content, peroxide value, and volatile basic nitrogen), specific energy consumption (kWh/kg H_2O removed), process repeatability (coefficient of variation $\leq$ 2.1%), and labor intensity (full-time equivalent per production line). The results are summarized in Table 13.

Table 13. Comparison of performance between traditional hot air drying process and improved vacuum low-temperature drying process.

Benchmark	Traditional Hot Air Drying Process	Improved Vacuum Low-Temperature Drying Process	Increase Margin
Heating temperature	110 °C	65 °C	reduce 40.9%
Drying time	120 min	75 min	shorten 37.5%
Protein content of fish meal	58.2%	64.2%	enhance 10.3%
Energy consumption per unit product	120 kWh per ton	85 kWh per ton	reduce 29.2%
Operator allocation	2 people	0.5 person per machine	Reduction in labor costs 75%

The optimized process demonstrated marked advantages across all dimensions. (1) Regarding product quality, the low-thermal-load environment effectively suppressed irreversible protein denaturation and lipid peroxidation, resulting in a 6.6% absolute increase in crude protein content (from 60.2 wt% to 64.2 wt%) and a 42% reduction in peroxide value relative to the hot air control. (2) Regarding process efficiency and energy performance, the drying cycle time decreased by 37.5% (from 120 min to 75 min), while specific energy consumption declined by 29.2% (from 2.84 to 2.01 kWh/kg H_2O), directly supporting decarbonization targets. (3) Regarding operational economics and automation, fully automated parameter control reduced the labor requirement from 2.0 to 0.5 full-time equivalents per production line—a 75% reduction—while improving setpoint adherence ($\pm$0.3 °C, $\pm$0.002 MPa) and eliminating manual intervention during drying cycles.

6. Conclusions

This study presented a vacuum low-temperature fish meal dryer designed to optimize structural integrity, enhance drying efficiency, and synergistically tune process parameters. Hardware innovations include a three-zone differentiated heating coil, a wear-resistant protective structure, and an optimized vacuum transfer bin. By integrating COMSOL Multiphysics simulations with response surface methodology (RSM), this work achieved co-optimization of hardware design and operational control. It systematically addressed persistent industry challenges, including low protein retention, suboptimal drying efficiency, and poor reliability of conventional fish meal dryers. Structural validation employed static analysis, thermo-structural coupling simulation, and thermal fatigue assessment to quantitatively evaluate performance. Using Atlantic cod (*Gadus morhua*) fish meal as the model feedstock, a three-factor, three-level RSM experiment was conducted to identify the optimal process conditions.

The results demonstrate that the optimized three-zone heating coil reduced the axial temperature gradient from 8.6 °C/m to 6.2 °C/m; coil stiffness increased by 20%, while peak stress decreased by 40.3%. The thermal fatigue life extended from 2–3 years to over 10 years. The optimal process parameters were 65 °C, 0.08 MPa, and 75 min. Under these conditions, the drying cycle shortened by 37.5%, specific energy consumption dropped by 29.2%, and the protein content rose by 6.6%. Labor costs decreased by 75%. Collectively, these outcomes confirm that integrated structural optimization and parameter matching significantly improve drying efficiency, product quality, and equipment reliability.

This study has several limitations. First, experimental validation was conducted exclusively on Atlantic cod fish meal; applicability to low-value fish species and aquatic by-products remains unverified. Second, simulations and experiments were performed under batch mode assumptions; continuous production dynamics (e.g., material flow rate and transient heat–moisture transfer) were not modeled or tested. Third, the quality evaluation framework covers the protein content and moisture but lacks comprehensive metrics for flavor profile, freshness indices (e.g., TVB-N or TMA), and lipid oxidation stability (e.g., PV or TBARS), limiting holistic quality assessment.

Future research should focus on three directions: (1) expanding the raw material scope to develop a generalized process parameter library for diverse marine biomass feedstocks; (2) implementing dynamic multiphysics simulation and pilot-scale validation of continuous production lines, including coordinated control of feeding, drying, and discharge; and (3) establishing a multidimensional quality evaluation system integrating nutritional integrity, sensory attributes, and food safety indicators, enabling real-time adaptive regulation via embedded intelligent sensors and machine learning algorithms. These advances will accelerate the scalable and intelligent industrial deployment of vacuum low-temperature fish meal drying technology.

Author Contributions: Conceptualization, W.W. and R.L.; Methodology, W.W.; Software, X.C. and D.L.; Validation, W.F.; Formal analysis, X.C.; Investigation, X.C., W.F. and D.L.; Resources, W.F. and D.L.; Data curation, W.F.; Writing—original draft, X.C.; Writing—review & editing, X.C., W.W. and R.L.; Visualization, X.C.; Supervision, W.W. and R.L.; Project administration, W.W. All authors have read and agreed to the published version of the manuscript.

Funding: Zhejiang Provincial Major Science and Technology Program Project (Grant No. 2026LDC01047, GZ). Zhoushan Dinghai District Science and Technology Program Project (Grant No. 2024C31003).

Data Availability Statement: Data are contained within the article.

Conflicts of Interest: Authors Wuwei Fang and, Danyu Li were employed by the company Zhejiang Longyuan Sifang Machinery Manufacture Co., Ltd. Author Rongsheng Lin was employed by the company JURONG ENERGY (XINJIANG) Co., Ltd. The remaining authors declare that the research was conducted in the absence of any commercial or financial relationships that could be construed as a potential conflict of interest.

References

1. Wang, J.Q.; Zhang, B.; Zhang, B.T.; Li, A.Q. Classification, processing technology, and quality control measures of fish meal. *Feed China* **2012**, *15*, 25–27.
2. Ministry of Agriculture and Rural Affairs of the People's Republic of China. *China Fisheries Statistical Yearbook*; China Agriculture Press: Beijing, China, 2024.
3. Duan, D.Y.; Chen, P.; Chen, X.J.; Qin, C.X. Construction of a grey system-based prediction model for Peruvian anchovy resources. *J. Shanghai Ocean Univ.* **2018**, *27*, 284–290.
4. Zhang, X.H.; Gao, H.C.; Chen, P. Fluctuation characteristics of Peruvian anchovy resources at different time scales. *J. Shanghai Ocean Univ.* **2022**, *31*, 761–769.
5. Ding, Q. Sustainable Utilization and Vulnerability Evaluation of Global Marine Fishery Resources. Master's Thesis, Shanghai Ocean University, Shanghai, China, 2017.

6. Leng, X.J. Research and application of low-fishmeal aquatic feed. *Feed Ind.* **2020**, *41*, 1–8.
7. Wang, Z.W.; Zhang, W.Y.; Cui, J.H. Research progress and prospect of vacuum drying technology. *Chem. Mach.* **2021**, *48*, 321–325.
8. Ren, J.Y.; Chen, W.D.; Wang, L.J.; Tian, X.Q.; Zhang, J.L. Discussion on the development trend of grain drying equipment. *Agric. Mach. Use Maint.* **2025**, *12*, 70–74.
9. Xu, C.J. Current status and prospects of green and low-carbon technologies for grain drying. *Agric. Eng.* **2024**, *14*, 94–101.
10. Liu, D.T.; Liu, Z.Y.; Liu, S.D.; Feng, T. Simulation of slow drying in porous media based on COMSOL Multiphysics. *Food Mach.* **2024**, *40*, 108–115.
11. Meng, Q.T.; Liang, C.H.; Zheng, P.; Zhang, H. Hot-air drying model and heat–mass transfer analysis of sweet potato slices. *Cereal Food Ind.* **2025**, *32*, 30–35.
12. Guo, W.B.; Li, Y.; Huang, C.H.; Du, J.Q.; Qian, S.Z.; He, Z.M.; Gao, J.J. Physical field analysis and structural optimization of drying chambers based on COMSOL. *Chin. Agric. Sci. Bull.* **2022**, *24*, 90–98.
13. Wei, L.N.; Li, L.H.; Hao, S.X.; Huang, H.; Yang, X.Q.; Xiang, H.; Zhao, Y.Q.; Cen, J.W.; Wei, Y. Effects of heat pretreatment on freeze-drying of tilapia. *Food Sci.* **2023**, *44*, 51–59.
14. Wei, J.; Wang, E.J.; Wei, M.Q.; Zhang, X.J.; Chen, Y.M. Optimization of low-temperature vacuum drying process of goji berries based on response surface methodology. *China Food Addit.* **2024**, *35*, 138–145.
15. Zheng, Y.P.; Wang, C.T.; Zheng, G.H. Application research of continuous vacuum dryers in fish meal processing. *J. Zhejiang Ocean Univ. (Nat. Sci. Ed.)* **2014**, *33*, 534–537.
16. Li, F.X.; Li, Y.X.; Xu, X.M. Design and simulation analysis of variable-pitch helical structures. *Packag. Eng.* **2019**, *40*, 214–221.
17. Hou, Y. Research on Heat Transfer Characteristics and Mechanical Properties of Variable-Pitch Twisted Heat Exchanger Tubes. Master's Thesis, Taiyuan University of Science and Technology, Taiyuan, China, 2026.
18. Luo, Y.Z.; Zhang, C.Q.; Luo, H.R.; Chen, L.P. Calculation of thin-walled cylinders under external pressure. *Mach. Res. Appl.* **2017**, *30*, 125–127.
19. Huang, Y.; Lin, H.Z.; Du, C.C. Relative error analysis of strength calculations for thin-walled cylinders. *J. Chang. Univ.* **2019**, *29*, 10–13+45.
20. Zhang, Z.P.; Wu, C.D.; Zhang, B.; Chu, X.M.; Wang, X.; Hu, X.K.; Yang, T. Design and finite element simulation optimization of rotating brackets for near-ground crop imaging [DB/OL]. *Trans. Chin. Soc. Agric. Mach.* **2026**. Available online: https://kns.cnki.net/kcms2/article/abstract?v=yLAonKG4u-T7P4257RT6A5WAS-eKV9id-LRtlAWy1zKbWipDUXhOU6PpgV3zToS-mrMIEJO6LuxHEaV0CL-2cXnK_6Q8JvGkIolh8vVGf68yFZ2zYCZlDe2b9FBVDgXpHHulykzEKM5ZUAHaAFp-I9rSdqB0uI2TDM0njjJbRPYmSV8ZKa5QdQ==&uniplatform=NZKPT&language=CHS (accessed on 14 May 2026).
21. Xu, Z.L. *Elastic Mechanics*, 5th ed.; Higher Education Press: Beijing, China, 2016.
22. Sun, Y.D.; Liu, X.Y.; Liu, H.; Liu, Y.J.; Wu, K. Stress state equation of surrounding rock in marine soft soil shield tunnels and its coupled solution method. *Munic. Technol.* **2026**, *44*, 55–65+96.
23. Sui, J.M. Research on Coupled Heat Transfer Characteristics of Multi-Physics Fields in Porous Deposition Products Based on CRUD. Master's Thesis, Northeast Electric Power University, Jilin City, China, 2025.
24. Xu, L.W. Research on Transformer Modeling and Fault Diagnosis Algorithms Based on COMSOL. Master's Thesis, Guizhou University, Guiyang, China, 2025.
25. *GB/T 150.1–2024*; Pressure Vessels—Part 1: General Requirements. China Standards Press: Beijing, China, 2024.
26. Yang, S.M. *Heat Transfer*, 5th ed.; Higher Education Press: Beijing, China, 2019.
27. Liu, Q.S.; Xu, Z.P.; Chen, X.K.; Li, S.H. Simulation analysis of insulation materials in high-temperature environments based on COMSOL thermal design. *J. Phys. Conf. Ser.* **2025**, *1*, 012007. [CrossRef]
28. Juckers, A.; Potschka, A. Advanced freeze-drying modeling: Validation of a sorption–sublimation model. *ACS Omega* **2025**, *10*, 16962–16976. [CrossRef]
29. Huang, Y.J.; Zhou, S.Z.; Li, N. Fatigue performance testing of high-pressure manifold materials and fitting of P–S–N model curves. *J. Yangtze Univ. (Nat. Sci. Ed.)* **2024**, *21*, 55–61.
30. Zhao, J.W.; Tao, Y.R.; Pei, J.X.; Zhang, Y. Research on fatigue life of SUS304 stainless steel spot-welded joints. *J. Mech. Strength* **2023**, *45*, 1005–1010.
31. Fan, S.G.; Zhang, S.H.; Meng, C. Experimental study on high-temperature mechanical properties of S30408 austenitic stainless steel. *Eng. Mech.* **2017**, *34*, 167–176+186.
32. Zheng, J.D.; Li, L.; Tian, L.Z.; Fan, J.L. Effect of annealing temperature on fatigue damage evolution behavior of 304 stainless steel. *Hot Work. Technol.* **2025**, *54*, 29–33.
33. FKM. *Guidelines for Design Proofs of Machine Parts by Calculation*; VDMA Verlag: Frankfurt am Main, Germany, 2021.
34. Erinosho, T.O.; Li, P.; Truman, C.E.; Smith, D.J. Pressure, temperature, and dwell time effects on fatigue life in 304 stainless steel using a R5-based mechanistic fatigue model. *Procedia Eng.* **2016**, *160*, 191–198. [CrossRef]
35. Wang, S.L.; Pan, J.J.; Dong, R.X. Research on the effects of different drying parameters on the quality of Chimonanthus salicifolius tea. *Zhejiang Agric. Sci.* **2023**, *64*, 846–849.

36. Han, F.; Wu, W.F.; Liu, Z. Simulation experiment system for continuous grain drying processes and process control. *Cereal Oil Sci. Technol.* **2023**, *31*, 83–89.
37. Yu, X.; Zhang, Z.P.; Xie, P.X. Development of an intelligent temperature control system for continuous microwave dryers. *Autom. Technol. Appl.* **2021**, *40*, 21–26.
38. Zhang, S.S.; Zheng, Y.; Guo, Q.Y. Vacuum drying characteristics of Antarctic krill powder and its impact on quality. *Packag. Eng.* **2024**, *45*, 91–100.
39. Li, X.; Liu, Z.Q.; Zhang, B.B. Effects of cottonseed concentrated protein replacing fishmeal on the quality of low-starch slow-sinking extruded feed pellets and optimization of process parameters. *J. Hydrobiol.* **2025**, *49*, 145–156.
40. Wen, H.X.; Gao, J.; Yu, Z.J. Effects of vacuum low-temperature drying process parameters on the quality of dried jujube slices. *Food Ind.* **2016**, *37*, 107–110.
41. Kamau, B.K.; Atitwa, E.B.; Mwithiga, G. Modeling and optimization of quality indicators of blanched and dried cowpea leaves using response surface methodology (RSM). *Heliyon* **2026**, *12*, e44642. [CrossRef]
42. Li, J.X.; Yu, X.Y.; Yang, L.W.; Wu, X.H. Research on hot-air drying characteristics and optimization of drying process parameters of alfalfa [DB/OL]. *Chin. Agric. Sci. Bull.* **2026**. [CrossRef]
43. Yang, L.; Yang, C.Y.; Cao, S.T.; Guan, R.; Zhang, B.; Yao, X.; Wang, Q.; Dong, W.; Huang, Y. Optimization of drying parameters and texture properties of winter jujube slices using radio frequency combined with hot air. *Front. Nutr.* **2025**, *11*, 1523078.

Disclaimer/Publisher's Note: The statements, opinions and data contained in all publications are solely those of the individual author(s) and contributor(s) and not of MDPI and/or the editor(s). MDPI and/or the editor(s) disclaim responsibility for any injury to people or property resulting from any ideas, methods, instructions or products referred to in the content.